International Journal of Plasticity 151 (2022) 103215

Contents lists available at ScienceDirect

International Journal of Plasticity

journal homepage: www.elsevier.com/locate/ijplas

Dynamic strain ageing in an AlMg alloy at different strain rates and temperatures: Experiments and constitutive modelling

Jianbin Xu [a,b,*], Bjørn Holmedal [a], Odd Sture Hopperstad [b], Tomáš Mánik [a], Knut Marthinsen [a]

[a] Department of Materials Science and Engineering, Norwegian University of Science and Technology (NTNU), Alfred Getz vei 2, NO-7491 Trondheim, Norway

[b] Centre for Advanced Structural Analysis (CASA), Norwegian University of Science and Technology (NTNU), Richard Birkelands vei 1a, NO-7491 Trondheim, Norway

ARTICLE INFO

Keywords:
Aluminium alloys
Constitutive behaviour
Dynamic strain ageing
Critical strain
Strain rate sensitivity
PLC domain

ABSTRACT

Uniaxial tension tests at strain rates from 10^{-4} to 10^{-1} s^{-1} and temperatures from 298 to 418 K are performed to study the dynamic strain ageing (DSA) of an AA5182-O sheet. Digital image correlation (DIC) is used to obtain the stress-strain curves and characterize the heterogenous deformations. A constitutive model based on the mechanical threshold stress (MTS) framework is then proposed and used to calculate the stress–strain response at different strain rates and temperatures. The modified MTS model captures the dependence of the strain rate sensitivity (SRS) on strain, temperature and strain rate both inside and outside the Portevin–Le Chatelier (PLC) domain. Special attention is paid to re-interpret the occurrence of stress serrations. It is found that the competition between work hardening and DSA leads to different jerky flow scenarios. The modified MTS model is used to predict the PLC domain as a function of strain rate and temperature. To further test the validity of the model at various temperatures and alloys, it is also approximately calibrated to Ni-based superalloys, for which it captures earlier reported behaviour at elevated temperatures.

1. Introduction

The intrinsic physical properties of a metallic material play an important role during plastic deformation but also the external loading conditions, such as strain rate and temperature, strongly influence the stress-strain behaviour. It is thus of great importance to obtain a profound understanding of the underlying mechanisms of plastic deformation over different temperatures and strain rates and to develop physically-based constitutive models for simulation of plastic forming processes.

For pure metals, dislocations are considered as the carriers of plastic deformation at the micro-scale level. Under load, the dislocations will move rapidly until encountering obstacles. It is widely accepted that the obstacles can be categorized into two main types: the strain rate and temperature independent interactions between the dislocations with long-range barriers such as grain boundaries, and the strain rate and temperature dependant interactions with short range obstacles (Follansbee and Kocks, 1988; Holmedal, 2007; Picu, 2004). For face-centred (fcc) metals, the forest dislocations are considered as the dominant short-range obstacles (Pham et al.,

* Corresponding author.
E-mail addresses: jianbin.xu@ntnu.no (J. Xu), bjorn.holmedal@ntnu.no (B. Holmedal), odd.hopperstad@ntnu.no (O.S. Hopperstad), tomas.manik@ntnu.no (T. Mánik), knut.marthinsen@ntnu.no (K. Marthinsen).

https://doi.org/10.1016/j.ijplas.2022.103215
Received 22 June 2021; Received in revised form 26 December 2021;
Available online 7 January 2022

2015). At finite temperatures, thermal activation will play an important role in lowering the required stress for the dislocation to overcome the as-built energy barriers. Besides, the temperature and strain rate will also influence the dislocation evolution, especially the dynamic recovery in the late stage of the deformation (Nes, 1997). Overall, the microscopic dislocation movement and the macroscopic stress-strain curves are found to significantly rely on the external imposed strain rate and temperature.

For alloys, the introduction of the extra elements can considerably strengthen the materials and improve the mechanical properties. Unfortunately, dynamic strain ageing (DSA) in a certain range of strain rate and temperature might lead to the loss of deformation stability, which in a tension test manifests itself by a serrated stress-strain curve and localized deformation bands moving back and forth across the gauge region of the sample. This phenomenon is known as the Portevin–Le Chatelier (PLC) effect (Portevin and Le Chatelier, 1923). During the plastic flow, the dynamically diffusing solute atoms will cluster around the dislocations that are temporally arrested at the obstacles and provide an extra barrier for the dislocation motion. Since diffusion is a strain rate and temperature dependant process, it will inevitably bring additional complexity in the simulation of the thermomechanical behaviour of materials exhibiting the PLC effect.

Great efforts have been made to study the PLC effect during the last few decades, however, there is still no consensus amongst researchers about all fundamental issues, especially concerning the mechanisms of solute diffusion and the strengthening effects of the solute atoms. The most unique feature associated with DSA is the negative steady-state strain rate sensitivity (nSRS) (Kubin and Estrin, 1990), which implies that a local strain rate increase will lead to strain softening during the deformation and make the material more prone to deformation instabilities. Cottrell and Bilby (1949) first proposed that the solute atmosphere will cluster around the dislocations due to the size misfit introduced by the foreign atoms and nSRS will appear when the dislocation escape from these pinning points. Later, it was suggested that the dislocations will move in a stop-go manner, and bulk or pipe diffusion will occur during the waiting time of the mobile dislocations, while they are temporarily arrested (McCormick, 1972; Sleeswijk, 1957; Van den Beukel, 1975). However, it was realized that conventional solute diffusion is too slow to provide sufficient strengthening, see e.g. the discussion in Picu (2004). Recently, a single-atomic-hop cross-core diffusion mechanism was proposed for substitutional alloys, from atomistic simulations, and a corresponding analytic expression for the solute diffusion as a function of strain rate and temperature was developed (Curtin et al., 2006).

Temperature and strain rate can also strongly affect the occurrence of the deformation instability. A remarkable feature related to the PLC effect is that the instability occurs after a critical strain level, which depends on the applied strain rate. At a given temperature, the critical strain increases with increasing strain rate in tensile tests in the high strain rate range, which is referred to the 'normal' behaviour, while the critical strain decreases with increasing strain rate in the low strain rate range, which is called the 'inverse' behaviour (Brechet and Estrin, 1995; Hähner, 1997). As a result, a U-shaped critical strain vs strain rate curve is obtained from experiments. Similarly, a temperature dependence of the critical strain has also been observed experimentally (Fu et al., 2012).

The variation of the critical strain with strain rate and temperature is attributed to the vanishing of the SRS (Kubin and Estrin, 1990; Mulford and Kocks, 1979). It is widely accepted that solute atoms contribute negatively to the SRS and that this contribution will increase with strain. According to Van den Beukel (1975), the strain rate dependence of the critical strain is caused by the enhancement of solute diffusivity by deformation-induced vacancies. Besides, the mobile dislocation density, which increases with strain, also contributes to the SRS. Mulford and Kocks (1979) proposed that the solute atoms will mainly affect the junction strength of forest dislocations rather than the friction stress. Picu and Zhang (2004) validated this hypothesis by atomistic simulations, which show that pipe diffusion is too slow to produce significant strengthening of the temporarily arrested mobile dislocations. By considering the evolution of both the mobile and forest dislocation density with strain, Kubin and Estrin (1990) proposed a consistent explanation of the experimentally observed complex onset and termination of the jerky flow. It should be noted that this model implies that the SRS might not always decrease with deformation, and under certain conditions the SRS might change from negative to positive, resulting in the disappearance of the jerky flow.

At a constant temperature, the constitutive relation between the stress σ and the strain rate $\dot{\varepsilon}$ at a given level of strain ε can be described by an "N-shaped" curve (Penning, 1972; Sleeswyk, 1958). In the valley of this curve, at intermediate strain rates, the dislocation motion and solute diffusion have comparable time scales and a nSRS will be observed. Outside the valley, the SRS is positive as for materials not exhibiting the PLC effect. In tests at high strain rates, the thermal escape is much faster than the solute diffusion and the DSA will vanish, while a "fully-aged" state will arise at extremely low strain rates when there is enough time for diffusion to fully saturate the solute atmosphere around the dislocations. The shape of the σ-$\dot{\varepsilon}$ curve depends strongly on temperature. With increasing temperature, the valley of nSRS shifts in the direction of higher strain rates, due to the thermally favoured diffusion. Outside the PLC domain, the slope of the monotonically increasing σ-$\dot{\varepsilon}$ curve, i.e., the magnitude of the positive SRS, will increase with temperature according to thermal activation theory, i.e., as described by the MTS model (Kocks and Mecking, 2003). Capturing the temperature-dependant N-shaped σ-$\dot{\varepsilon}$ curve is challenging but pivotal to accurately predict the thermomechanical behaviour of alloys exhibiting DSA.

The thermomechanical behaviour of alloys exhibiting DSA and the PLC effect has been simulated in numerous studies. Phenomenological or semi-physically based models, see e.g. Rusinek and Rodríguez-Martínez (2009), Kabirian et al. (2014), Wang et al. (2015), Kreyca and Kozeschnik (2018), Voyiadjis et al. (2019), Voyiadjis and Song (2020) and Song et al. (2020), have been applied to simulate the stress-strain curves within the strain rate and temperature range where DSA prevails. The KEMC model, which is based on the work of Kubin and Estrin (1990) (KE) and McCormick (1988) (MC), has been applied in several studies, partly due to its easy implementation in finite element codes (Benallal et al. (2008); Klusemann et al. (2015); Ren et al. (2021)). In some studies, the parameters of the KEMC model are taken to be temperature dependant to model the stress-strain behaviour at different temperatures, e.g. Belotteau et al. (2009); Wang et al. (2012); Mansouri et al. (2016); Ren et al. (2017). Physically-based models derived from atomistic simulations have also been used to simulate the mechanical response in the DSA regime for different strain rates and temperatures

(Picu (2004); Soare and Curtin (2008); Keralavarma et al. (2014)).

Although a number of constitutive models have been utilized to describe the influence of DSA on the stress-strain behaviour, the quantitative agreement with experimental results is still far from satisfactory. This motivates the present study where the tensile behaviour of an AA5182-O alloy for different strain rates and temperatures within the DSA domain is systematically investigated. Firstly, an accurate physically-based constitutive model for DSA is proposed that captures the stress-strain responses of the alloy under both steady-state conditions and situations with varying strain rates. To this end, a modified version of the MTS model is developed. Secondly, extensive experimental studies, such as Mulford and Kocks (1979) and Picu et al. (2005), have been performed to investigate the evolution of the SRS; however, none of the existing models captures the complex dependence of the SRS on strain, temperature and strain rate both inside and outside the PLC domain. A comprehensive study of the evolution of the SRS and the factors influencing this evolution is provided here. Thirdly, the current work provides a novel consistent re-interpretation of the long-standing unsolved fundamental issue associated with the PLC effect, namely the occurrence of critical strains for the onset and termination of jerky flow. Finally, special attention is paid to the PLC domain as a function of strain rate and temperature, by applying the proposed physically-based constitutive model. Besides, an original digital image correlation (DIC) tensile test with an unprecedented ultimate acquisition frequency is conducted to track the localizations nearby the PLC boundary at high strain rates.

The paper is organized as follows. Section 2 presents the material and the experimental study. The proposed modified version of the MTS model is described in Section 3, whereas Section 4 outlines the parameter identification based on selected experimental data. Section 5 presents experimental and numerical results, the latter obtained with the modified MTS model, and provides a comprehensive discussion of various aspects of DSA and the PLC effect. Some main conclusions are drawn in Section 6.

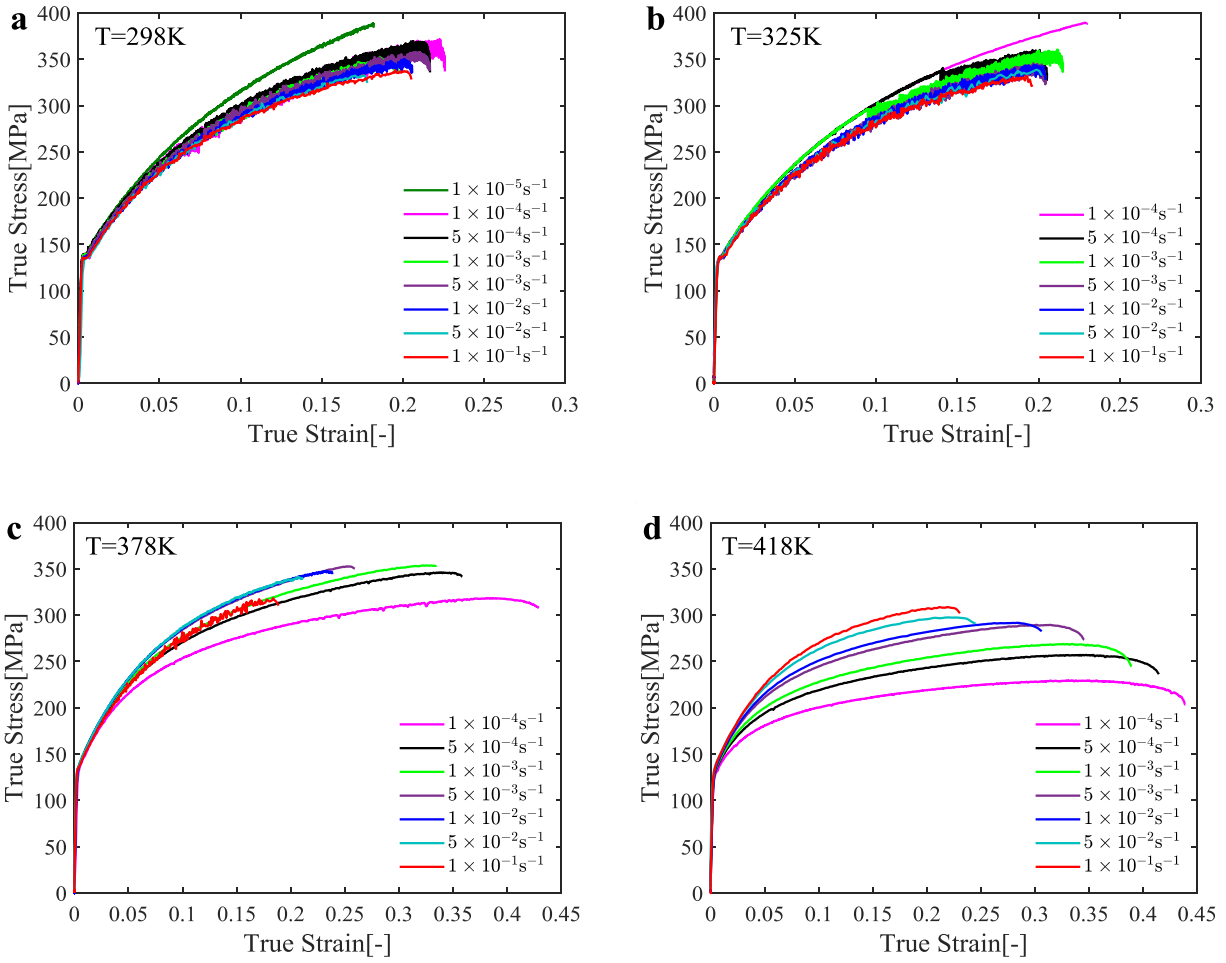

Fig. 1. Experimental stress-strain curves of AA5182-O at different strain rates and temperatures.

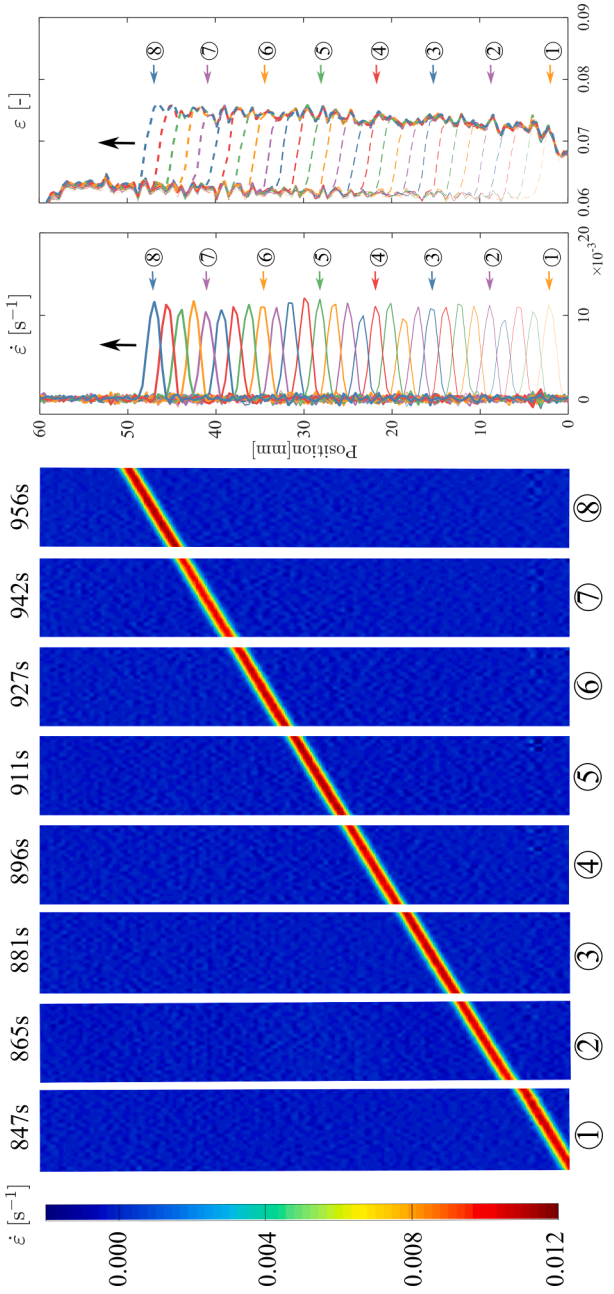

Fig. 2. Example of the PLC band propagation in a test with strain rate 10^{-4} s^{-1}at room temperature. The left figure shows the full-field strain rate maps, whereas the middle and right figures show the corresponding strain rate and strain distributions along the central axis of the specimen.

2. Material and experiments

2.1. Material

Specimens for tensile testing were machined from a thin sheet (1.2 mm) of the commercial aluminium alloy AA5182-O produced by casting, hot and cold rolling and subsequent annealing. The main alloying element is 4.55 wt.% Mg, together with Si (0.11 wt.%), Fe (0.21 wt.%), Cu (0.0215 wt.%), Mn (0.27 wt.%), Cr (0.0033 wt.%), Zn (0.005 wt.%) and Ti (0.01 wt.%). The tested material had a typical recrystallized and weakly textured microstructure with an average grain size of 11 μm. Dog-bone shaped specimens with a gauge area of 12 mm×1.2 mm×60 mm were cut by electrical discharge machining, with the tensile axis in the rolling direction.

2.2. Experimental procedures

Uniaxial tension tests were carried out at room temperature and elevated temperatures by using a servo-hydraulic MTS testing machine with 100 kN capacity. Constant crosshead speeds corresponding to nominal strain rates ranging from 10^{-4} s^{-1} to 10^{-1} s^{-1} were applied in the tests. Four temperatures, namely 298 K, 325 K, 378 K and 418 K, are selected to perform the tests. Three parallel tests were conducted for each combination of strain rate and temperature. It should be stated that, in order to minimize the influence from other potential mechanisms, such as recovery and solute drag, all testing temperatures are below $0.5T_m$, where T_m is the melting temperature, at which dislocation glide is considered as the main deformation mode (Chen et al., 1998). In the tests at elevated temperatures, a heat chamber was used. The chamber was pre-heated for 1.5 h to ensure that both the chamber and grip holder had reached the desired temperature. In each individual test, the furnace was opened to clamp the specimen. Since it takes some time for the mounted specimen to reach the equilibrium temperature, a 2-min pre-warming of each sample was be applied before the tests. The temperature was measured with a thermocouple spot-welded to the specimen surface.

The digital image correlation (DIC) technique is widely used to characterize the non-uniform deformation of materials with the PLC effect (Swaminathan et al. (2015);Lee et al. (2021)). An in-house DIC software, developed by Fagerholt (2012), was used to obtain the strain field and to observe the PLC bands during the tests. The specimens were sprayed with an artificial black speckle pattern on a white-painted surface for the DIC software to track the displacement field of the specimen surface, from which the strain field was calculated. A high-speed CCD camera with resolution of 1397 dpi was utilized to acquire digital images with a frame rate from 1 frame/s to 1000 frames/s. The global strain was measured by tracking the elongation of a virtual extensometer with 60 mm gauge length along the tensile axis. The DIC system provided a synchronization between the series of images and the force signal from the load cell of the machine, and thus the stress-strain curve could be calculated. This non-contact technique could precisely detect the non-uniform deformation and the spatio-temporal behaviour of the PLC bands. Both strain and strain rate field maps were derived from analyses of the images acquired during the tests (Jacobs et al., 2019; Yuzbekova et al., 2017; Zavattieri et al., 2009).

2.3. Experimental results

2.3.1. Stress-strain curves

The stress-strain curves for different strain rates (10^{-4} s^{-1} to 10^{-1} s^{-1}) at four different temperatures are shown in Fig. 1. At room temperature (298 K) in Fig. 1a, one extra curve corresponding to the strain rate of 10^{-5} s^{-1} is also displayed to show the lower strain rate boundary where the jerky flow disappears. Several extra experiments, although not shown here, were also conducted with strain rate between 10^{-4} $s^{-1}$and 10^{-5} s^{-1} to detect this boundary. At all strain rates, the yield stress is about 136 MPa and not rate sensitive. A yield plateau is observed right after the elastic loading, after which a negative steady-state SRS is displayed, i.e., the stress level decreases with increasing strain rate within the PLC domain. The stress serrations are very pronounced after the critical strain has been reached. Moreover, it is observed that the amplitude of the serrations is quite high at low strain rates, while light serrations are observed in the high strain rate regime.

At 325 K, the stress-strain curves are very similar to those at room temperature, see Fig. 1b. It is interesting to note that the lower strain rate boundary for the jerky flow changes from 10^{-5} s^{-1} at room temperature to 10^{-4} s^{-1} at 325 K. This provides a strong evidence of the temperature's influence on the strain rate domain within which the PLC effect prevails.

At 378 K, the strong serrations disappear at all but one strain rate, see Fig. 1c. As the strain rate is increased, a transition from positive to negative steady-state SRS takes place, and the negative steady-state SRS is only observed at the highest strain rate of 10^{-1} s^{-1}. At this strain rate, jerky flow is clearly evident. It is further seen that the stress-strain curves at strain rates between 5×10^{-3} $s^{-1}$and 5×10^{-2} s^{-1} almost overlap due to the transition from positive to negative steady-state SRS, whereas the tensile test at the lowest strain rate of 10^{-4} s^{-1} has a markedly lower stress level than the other tests.

At the highest temperature of 418 K, see Fig. 1d, all curves are quite smooth. From the DIC analyses, it is found that none of the tests at this temperature shows any sign of the PLC effect. A lower stress level but higher ductility is obtained in these tests compared to the tests at the other three temperatures. The initial yield stress is only slightly lower (~130 MPa) and still not rate sensitive. After yielding, the stress-strain curves at the different strain rates are much more dispersed than at the other temperatures, and the positive steady-state SRS is apparent at this temperature.

2.3.2. PLC bands

Fig. 2 shows the full-field strain rate maps at eight time-instants obtained by the DIC technique. The PLC band front is inclined at an

angle around 58° to the loading direction, which is comparable to previous experimental and numerical studies (Benallal et al., 2008; Ren et al., 2021). A well-defined localization band that nucleates nearby the grip end and propagates towards the other side of the specimen, is observed in these images. The plot in the middle shows strain rate distributions along the central axis of the tensile specimen at the corresponding time instants, with a strain rate peak in the centre of the PLC band front. The strain rate is low outside the PLC band front, which indicates elastic straining or stress relaxation. The plot to the right in Fig. 2 shows the strain profile across the specimen. As the band propagates, the area behind of the band accumulates a higher strain, while the area in front of the band is yet to deform plastically.

3. Constitutive modelling

3.1. The MTS model

Plastic deformation of polycrystalline aggregates is caused by the motion of dislocations. The strength comes from the barriers that resist the dislocation motion, which can be classified as long-range temperature-independent athermal barriers and short-range temperature-dependant thermal barriers. It has been shown that the mechanical threshold stress (MTS) can be used as the representative state variable for the internal microstructure of a material (Follansbee and Kocks, 1988; Kocks and Mecking, 2003). In this study, the main emphasis is on the material's constitutive behaviour in terms of the flow stress as a function of the strain, strain rate and temperature, assuming that the elastic strain is negligible and therefore omitted. A crystal plasticity framework is utilized here to relate the macroscopic flow stress σ and plastic strain rate $\dot{\varepsilon}$ to the resolved shear stress τ and shear strain rate $\dot{\gamma}$ on the slip planes by the Taylor factor, i.e., $\sigma = M\tau$ and $\dot{\varepsilon} = \dot{\gamma}/M$. Here, $M = 3$. In the MTS model, the critical resolved shear stress is expressed as:

$$\tau = \tau_0 + \tau_a + \tau_f = \tau_0 + \tau_a + \frac{\mu}{\mu_0} s(\dot{\gamma}, T)\widehat{\tau}_f \tag{1}$$

Here, τ_a is the dynamic strain ageing stress, or the ageing stress for short, τ_0 is the athermal stress, μ_0 is the shear modulus at 0 K, and μ is the shear modulus at temperature T, defined by:

$$\mu(T) = \mu_0[1 - D_0 / (\exp(T_0 / T) - 1)] \tag{2}$$

where D_0 and T_0 are empirical constants. The mechanical threshold stress $\widehat{\tau}_f$ is the part of the critical resolved shear stress at 0 K that is controlled by the dislocation-dislocation interactions. The mechanical threshold stress can be expressed in terms of the dislocation density as (Taylor, 1934):

$$\widehat{\tau}_f = \alpha\mu b\sqrt{\rho} \tag{3}$$

where α is the interaction strength, b is the magnitude of the Burgers vector. It should be stated that the dislocation density and the associated evolution law are commonly adopted in the MTS model (Holmedal, 2007); however, the mechanical threshold stress is chosen in the current work to simplify the parameter identification. The strain rate and temperature dependant pre-factor $s(\dot{\gamma}, T)$ depicts the obstacle profile of the short-range temperature-dependant thermal barriers. According to Kocks and Mecking, 2003, an algebraic form for the activation energy yields a pre-factor $s(\dot{\gamma}, T)$ expressed as:

$$s(\dot{\gamma}, T) = \left\{1 - \left[\frac{kT}{g_0\mu b^3}\ln\left(\frac{\dot{\gamma}_0}{\dot{\gamma}}\right)\right]^{1/q}\right\}^{1/p} \tag{4}$$

Here, k is the Boltzmann constant, g_0 is the normalized structure evolution energy, $\dot{\gamma}$ is the shear strain rate, $\dot{\gamma}_0$ is the reference shear strain rate, and p and q are empirical constants.

3.2. Dynamic strain ageing stress

During deformation, the dynamically diffusing solute atoms will exert some extra resistance to the dislocation motion. During the temporary arrest of the dislocations, solute atoms will lead to additional pinning. An expression for this contribution was first given by Cottrell and Bilby (1949), and later modified by Louat (1981):

$$\tau_a = \tau_{a0}\ c = \tau_{a0}\left\{1 - \exp\left[-\left(\frac{t_a}{t_d}\right)^n\right]\right\} \tag{5}$$

where, τ_{a0} is the maximum or saturation ageing strength when dislocations are fully pinned, c is the relative solute concentration (i.e., 0 for no ageing and 1 for fully-aged state, respectively), t_a and t_d are the ageing time and characteristic diffusion time, respectively, and the exponent n equals 1/3 (Soare and Curtin, 2008). A "cross-core" diffusion model (Curtin et al., 2006), firstly proposed for substitutional Al-Mg alloys, is adopted here. Based on the atomistic simulations, the saturation binding energy per unit length is given as:

$$\Delta E_\infty = \frac{2c_0\overline{w}\Delta W}{\sqrt{3}b^2}\tanh\left(\frac{\Delta W}{2kT}\right) \tag{6}$$

where ΔW is the energy difference between the compression and tension sides of the slip plane, $\overline{w}$ is the width of the dislocation core and c_0 is the bulk solute concentration. The corresponding ageing stress is proportional to the value of the binding energy, i.e., $\tau_a = \alpha_c \Delta E/\overline{w}b$, where α_c is a coefficient for the energy variation along the core. By setting $\Delta W = g_{0w}\mu b^3$, the corresponding saturation ageing stress is:

$$\tau_{a0} = \frac{\alpha_c}{\overline{w}b}\Delta E_\infty = \frac{2c_0\alpha_c g_{0w}\mu}{\sqrt{3}}\tanh\left(\frac{g_{0w}\mu b^3}{2kT}\right) \tag{7}$$

where g_{0w} is the normalized energy difference. To facilitate the parameter identification, a reference saturation ageing stress $\widehat{\tau}_{a0}$ is introduced to replace the pre-factor in Eq. (7), and thus:

$$\tau_{a0} = \widehat{\tau}_{a0}\ \tanh\left(\frac{g_{0w}\mu b^3}{2kT}\right) \tag{8}$$

where, $\widehat{\tau}_{a0} = 2c_0\alpha_c g_{0w}\mu/\sqrt{3}$. Eqns.(5–8) gives the basic formulation for the dynamic strain ageing process with "cross-core" diffusion, for which more details can be found in Curtin et al. (2006) and Soare and Curtin (2008). It is found that the saturation ageing stress is a constant for a given alloy. However, as the dislocation density increases with plastic straining, the total length of the dislocation segments will increase and enhance the extra solution strengthening capability of the material. As a result, dynamic strain ageing will become more significant with increasing strain. To account for this effect, we assume a linear strain dependency of $\widehat{\tau}_{a0}$. Thus, we have:

$$\tau_{a0} = \left(\widehat{\tau}_{a00} + \widehat{\tau}'_{a00}\ \gamma\right)\ \tanh\left(\frac{g_{0w}\mu b^3}{2kT}\right) \tag{9}$$

where $\widehat{\tau}_{a00}$ and $\widehat{\tau}'_{a00}$ are two parameters to be fitted. As in Böhlke et al. (2009), the reference saturation ageing strength $\widehat{\tau}_{a0}$ is assumed to depend linearly on strain, even if a dependence of the dislocation density ρ would be more in line with the underpinning physical mechanisms. This modification is pivotal for describing the strain dependant characteristics of DSA. Further discussions of its influences will be given in the following sections.

The value of the relative solute concentration c varies between 0 (no ageing) and 1 (fully-aged) and is a function of the ratio between the ageing time t_a and the characteristic diffusion time t_d. At a constant strain rate, the ageing time t_a equals the average waiting time t_w, which is the time spent for dislocations to pass by the obstacles:

$$t_w = \frac{\Omega}{\dot{\gamma}} \tag{10}$$

where Ω is the elementary strain increment, which is assumed, for simplicity, to be a constant. For changing strain rates, McCormick (1988) proposed a relaxation function to describe the ageing time evolution by:

$$\frac{dt_a}{dt} = 1 - \frac{t_a}{t_w} \tag{11}$$

When the strain rate changes, the ageing time t_a will change towards the target value t_w. When the plastic strain rate vanishes, i.e., $\dot{\gamma} = 0$, the waiting time approaches infinity, and the ageing time equals the time increment, i.e., $dt_a = dt$. The intrinsic diffusion time is given by (Keralavarma et al., 2014; Soare and Curtin, 2008):

$$t_d = \frac{1}{3\nu_0}\exp\left(\frac{\Delta H_c}{kT}\right) \tag{12}$$

Here, ν_0 is the solute atom's reference vibration frequency, and ΔH_c is the activation enthalpy for cross-core diffusion, which is taken as $\Delta H_c = g_{0c}\mu b^3$ with g_{0c} being a normalized activation enthalpy.

3.3. Work hardening

The work hardening is expressed in terms of the evolution of the mechanical threshold stress $\widehat{\tau}_f$, or alternatively directly by the evolution of the dislocation density (Holmedal, 2007). A modified Voce law is applied here to calculate the evolution equation of $\widehat{\tau}_f$ (Follansbee, 2014):

$$\frac{d\widehat{\tau}_f}{d\gamma} = \theta_0\left(1 - \frac{\widehat{\tau}_f}{\widehat{\tau}_{fs}}\right)^\kappa \tag{13}$$

where θ_0 is the initial hardening rate and κ is an empirical constant. When $\kappa = 1$, this evolution function reduces to the Voce hardening rule, which represents an additive balance between the dislocation storage and dynamic recovery (Follansbee and Kocks, 1988). The saturation stress $\widehat{\tau}_{fs}$ is given by a phenomenological 'master curve' (Kocks and Mecking, 2003) as:

$$\widehat{\tau}_{\mathrm{fs}} = (1+\delta)\widehat{\tau}_{\mathrm{fs0}}\left\{1 - \left[\frac{kT}{g_{0\mathrm{s}}\mu b^3}\ln\left(\frac{\dot{\gamma}_{0\mathrm{s}}}{\dot{\gamma}}\right)\right]^{1/q_{\mathrm{s}}}\right\}^{1/p_{\mathrm{s}}} \tag{14}$$

where $\dot{\gamma}_{0\mathrm{s}}$ is the reference strain rate, $g_{0\mathrm{s}}$ is the normalized free energy, $\widehat{\tau}_{\mathrm{fs0}}$ is the strength of hard spots, and p_{s} and q_{s} are parameters defining the shape of the energy barrier. Different from the widely used power law form (Chen et al., 1998; Kreyca and Kozeschnik, 2018), the more general algebraic form is utilized in this work. Detailed discussions about the differences between the two forms will be provided in Section 5.1. A modification of the original version by Kocks and Mecking (2003) to account for the influence of the dynamic strain ageing on the dynamic recovery, and following Feng et al. (2017), we take:

$$\delta = R^{'}c \tag{15}$$

where δ defines the effect of solute atoms on the dynamic recovery, and $R^{'}$ is a dimensionless pre-factor (Soare and Curtin, 2008), which indicates the extent of the solute atoms' influence on the dislocation evolution.

4. Parameter identification

Due to the different microscopic mechanisms that are involved and their dependencies on both strain rate and temperature, it is impossible to identify all the parameters of the modified MTS model simultaneously. Here, the parameter values at room temperature are firstly calibrated and then applied as initial values for the fitting of the parameters when including all temperatures.

Tests at strain rates of 10^{-4} s^{-1}, 10^{-3} s^{-1}, 10^{-2} s^{-1}, 10^{-1} s^{-1} are selected as the data for the parameter identification. As shown in Fig. 1a and Fig. 1b, some of the experimental stress-strain curves are strongly serrated. Using a parametrization on the form $\sigma = \sigma_0 + \sum_{i=1}^{4} Q_{\mathrm{i}}(1 - \exp(-C_{\mathrm{i}}\varepsilon))$, where σ_0, Q_{i} and C_{i} are fitting constants, smoothened stress-strain curves were obtained by curve fitting. Due to the different type of serrations, different fitting strategies were used for tests at different strain rates. The upper envelope of the serrated curve was used for the tests at the low strain rates, while a standard least-squares fit was applied for tests at the intermediate and high strain rates. Original and smoothened stress-strain curves are compared in Fig. 3. Two extra tests at room temperature with strain rates of 10^{-5} s^{-1} and 1 s^{-1} were added to extend the dataset. The datapoints depicted by discrete circles with an interval of 1% strain are used as the experimental data in the curve fitting procedure. Smoothened stress-strain curves are obtained in the same manner for tests at elevated temperatures.

It should be kept in mind that when the strain rate is inside the PLC domain, the deformation is non-uniform. When this is the case, the strain rate, at which the plastic deformation takes place, is considerably higher than the overall strain rate of the sample, which makes it difficult to extract the stress-strain behaviour of the material without solving the boundary value problem e.g. by nonlinear finite element analysis. In the parameter identification, lower weight is given to the experimental datapoints which are extracted from the parts of the stress-strain curves with heavy serrations.

A least-squares fitting algorithm was used to minimize the deviation between the experimental datapoints and the calculated stress-strain curves. Fig. 4 shows both the experimental and calculated stress-strain curves, using the parameter set from the identification procedure given in the APPENDIX.

For a material not exhibiting DSA, the yield stress tends to decrease with increasing temperature or decreasing strain rate. In contrast, the yield stress of the Al-Mg alloy shows a very weak dependence on both the temperature and the strain rate, and this behaviour is well captured by the model as seen in Fig. 4a-d. At room temperature (298 K) where negative steady-state SRS is dominant, the calculated stress-strain curves are accurate at strain rates where only light serrations are observed, such as for the tests at

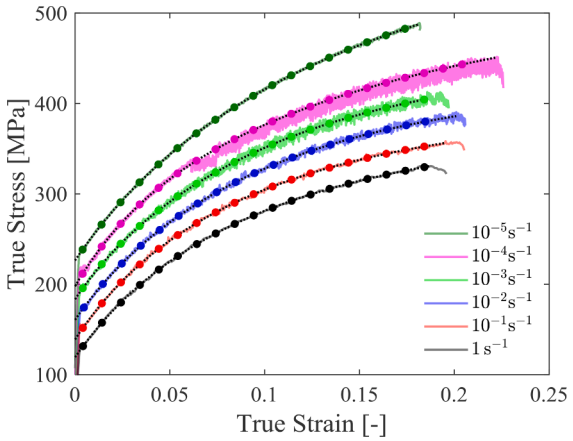

Fig. 3. Original (solid lines) and smoothened (dashed black lines) experimental stress-strain curves for different strain rates at room temperature. Discrete circles are data points used in the parameter calibration. To better distinguish them from each other, each curve is shifted successively upward by 20 MPa relative to the curve at 1 s^{-1}.

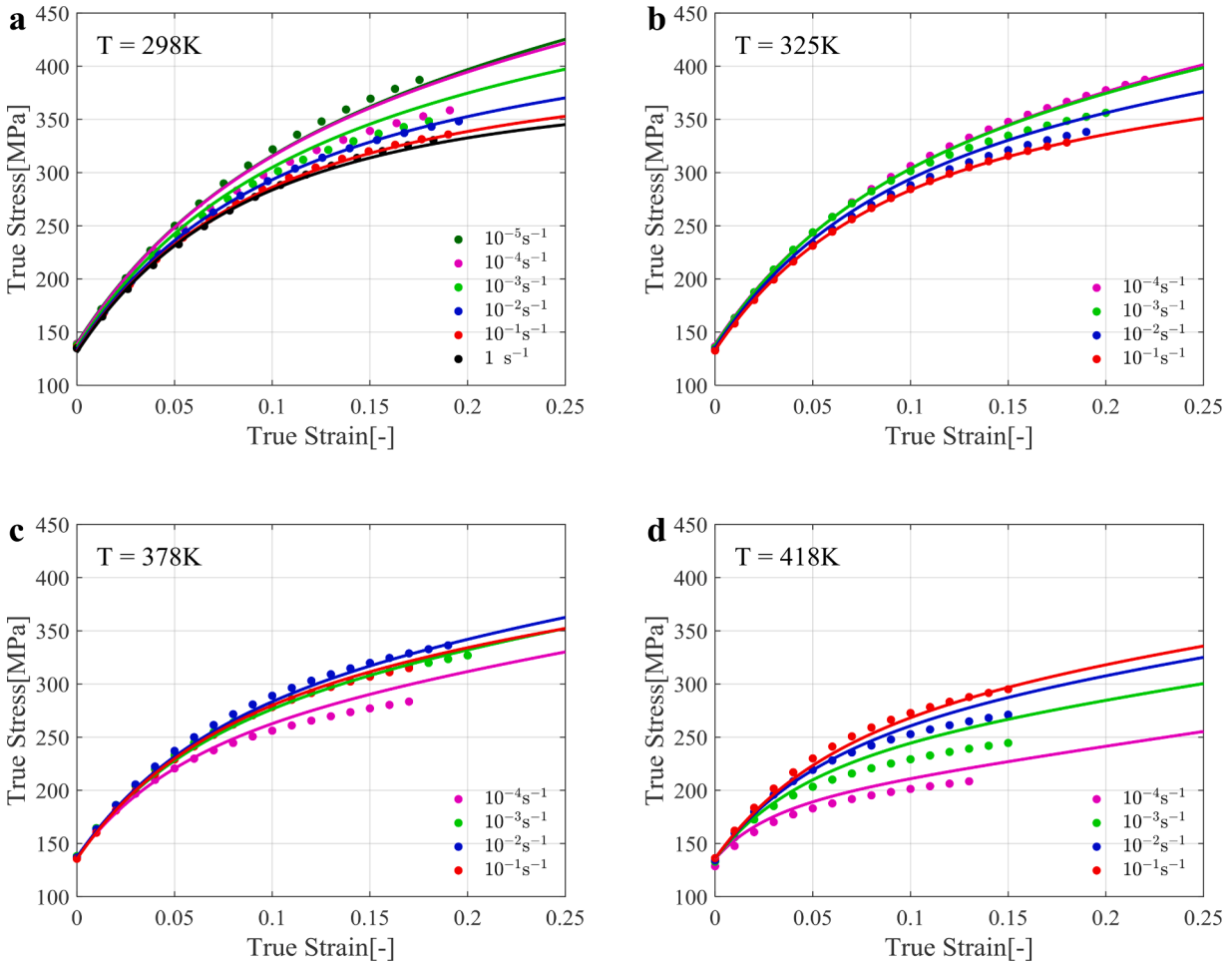

Fig. 4. Stress-strain curves for various strain rates and temperatures, where dots represent experimental datapoints and solid lines represent calculations.

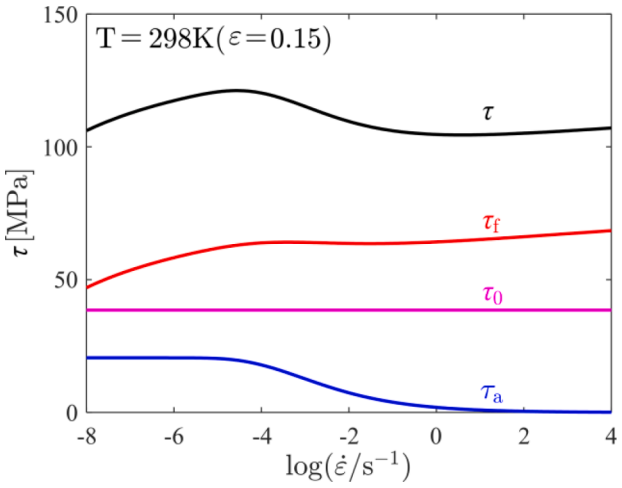

Fig. 5. Various predicted stress components vs strain rate at 15% strain and at room temperature.

1 s^{-1}, 10^{-1} s^{-1} and 10^{-2} s^{-1} in Fig. 4a. At lower strain rates, i.e., 10^{-3} s^{-1} and 10^{-4} s^{-1}, the calculations are accurate before the onset of strong serrations but then overestimate the stress level at higher strains. The reason for this is that the strain rate inside the PLC band is considerably higher than the overall strain rate, which reduces the work hardening for a material with negative steady-state SRS. Details about this overestimation of the stress can be found in Xu et al., 2022b. For the test at 10^{-5} s^{-1}, which is outside the PLC domain, the calculations are again in good agreement with the experimental data. Similar observations are made for the tests at 325 K in Fig. 4b and at 378 K in Fig. 4c.

At 418 K, all strain rates are completely outside the PLC domain, and the alloy exhibits substantial thermal softening and strong positive SRS. The calculated stress-strain curves are in good agreement with the experimental datapoints at this temperature in Fig. 4d. The experimental stress-strain curves in Fig. 4a-d show a transition from negative to positive steady-state SRS with increasing temperature. For example, the stress-strain curve for the test at strain rate 10^{-1} s^{-1} (plotted in red) has the second lowest stress level at room temperature (298 K) and the highest stress level at 418 K. This transition from negative to positive steady-state SRS is captured by the current model.

5. Results and discussion

5.1. Flow stress under steady-state conditions

The total stress, as defined in Eq. (1), has three components, namely the athermal stress τ_0, the ageing stress τ_a and the work hardening stress τ_f. Fig. 5 shows these three stress components at room temperature as functions of the strain rate, for a strain of 15%. The sum of the contributions from the stress components gives the typical non-monotonic "N-shaped" curve associated with the PLC effect. In the intermediate strain rate range, a negative slope of stress vs strain rate curve is obtained. The main reason for the nSRS and the corresponding PLC domain is the nSRS of τ_a, but also the positive SRS of τ_f vanish during this strain rate interval, due to the influence of the dynamic strain ageing on the dynamic recovery of the dislocations during straining.

Temperature and strain rate both influence the ageing process. The ageing stress at 15% strain is plotted against the strain rate for four different temperatures in Fig. 6a, and in Fig. 6b, the ageing stress against the temperature for different strain rates. Fig. 6b shows how the transition towards DSA is shifted towards larger temperatures with increasing strain rates, while Fig. 6a shows how the region of nSRS shifts in the direction of higher strain rates with increasing temperature. Faster solute diffusion at higher temperatures or sufficient time for diffusion at low strain rates promotes DSA. It is also noted from Fig. 6a that the saturation stress decreases with increasing temperatures. This is because the driving force for cross-core diffusion, or more specifically the binding energy difference between the tension and compression side of the dislocation core, will be lowered with increasing temperature (Curtin et al., 2006).

Temperature and strain rate also strongly influence the material's work hardening behaviour, which can be analysed by the Kocks-Mecking plots (Kocks and Mecking, 2003). In these plots, the work hardening rate, $\Theta = d\sigma/d\varepsilon$, is plotted against the effective stress, $\sigma - \sigma_0$, where σ_0 is the yield stress. Fig. 7 presents Kocks-Mecking plots of the experimental data at 418 K, i.e., outside the PLC domain, and at 298, i.e., inside the PLC domain. At 418 K, there is a marked influence of the strain rates on the work hardening behaviour, where the work hardening rate increases substantially with the increasing strain rate. At 298 K, the shape of the curves is quite similar to those at 418 K, but the work hardening is much less dependant on the strain rate. Moreover, the work hardening rate tends to decrease with increasing strain rate.

The distinct differences in the work hardening behaviour at 298 K and 418 K can be analysed by considering temperature and solute effects. Firstly, the saturated value of the mechanical threshold stress $\hat{\tau}_f$ decreases with increasing temperature and influences the shape of the Kocks-Mecking curves. It can be shown (Holmedal, 2007) that a power law form for $\hat{\tau}_{fs}$ is a simplified special case of Eq. (14), which is commonly adopted, e.g., for copper (Chen and Kocks, 1991), AA5182-O (Chen et al., 1998), Al-Mg (Kreyca and

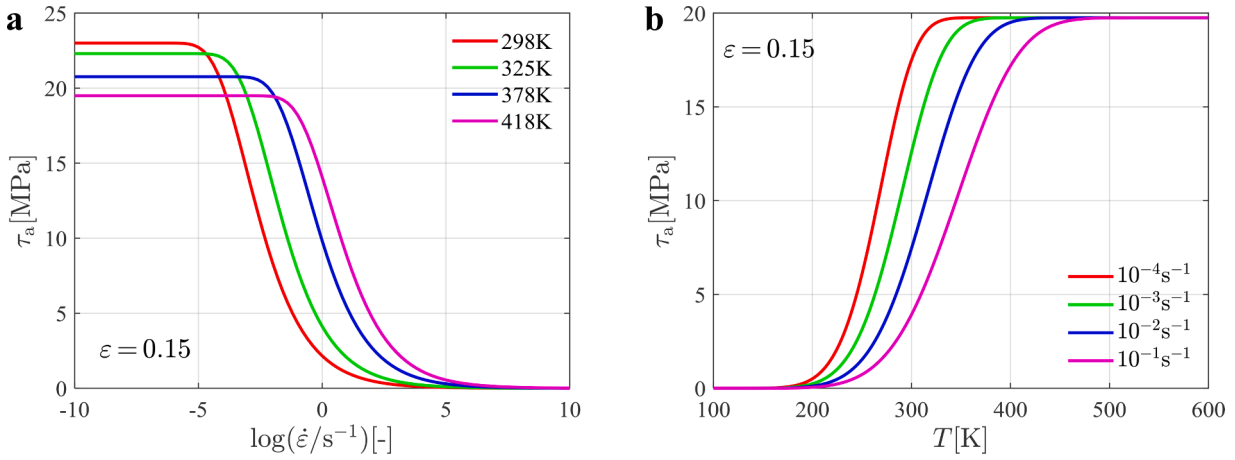

Fig. 6. The predicted ageing stress τ_a at 15% strain is plotted against (a) strain rate and (b) temperature.

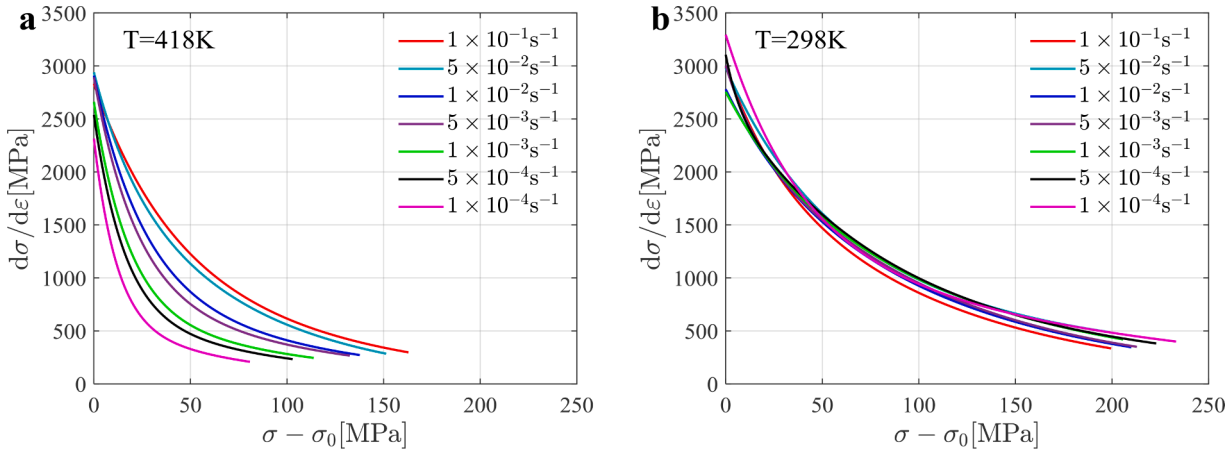

Fig. 7. Kocks-Mecking plots based on the experimental data at (a) 418 K and (b) 298 K.

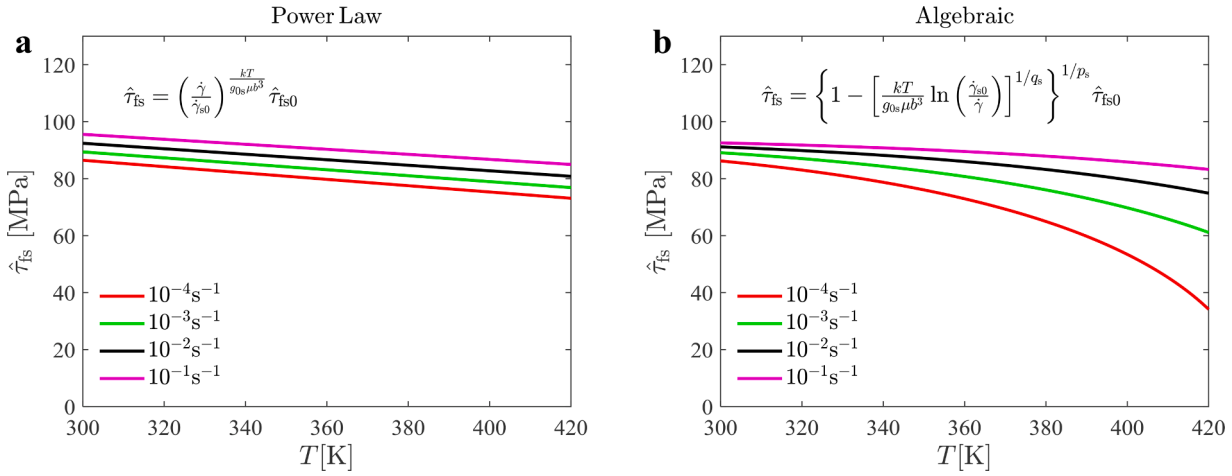

Fig. 8. Saturation stress calculated as a function of temperature without accounting for DSA: (a) power law form, and (b) algebraic form.

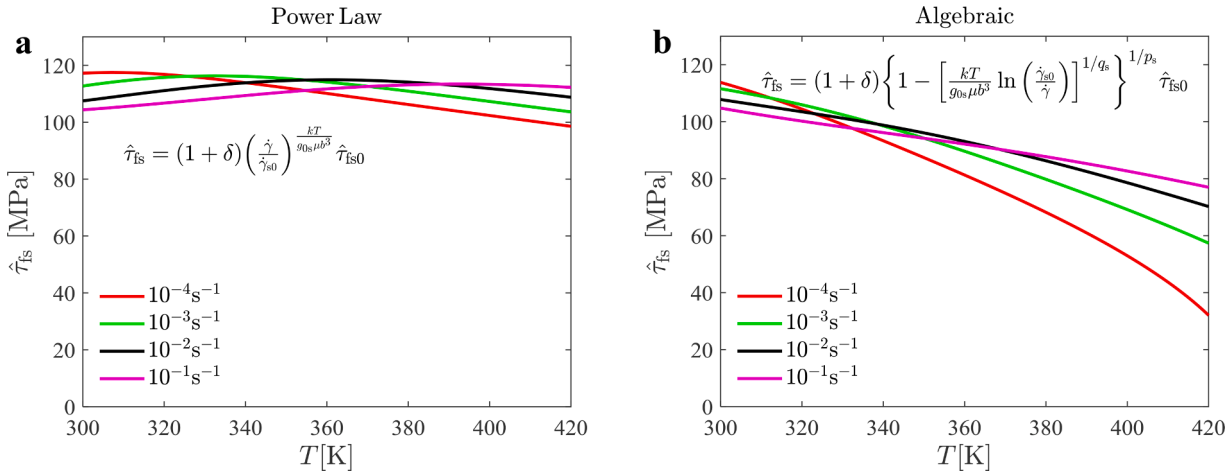

Fig. 9. Saturation stress calculated as a function of temperature when accounting for DSA: (a) power law form, and (b) algebraic form. The algebraic form in (b) is adopted in the current model.

Kozeschnik, 2018). Attempts were firstly made to fit the power law form to the AA5182-O alloy investigated here, for which the result is shown in Fig. 8a. However, the experimental stress-strain curves in Fig. 1 and the work hardening behaviour in Fig. 7 could not be properly captured by applying the simplified power law form. The phenomenological algebraic form (Holmedal, 2007; Kocks and Mecking, 2003) provided good fits and can be interpreted as a result of the temperature dependence of the stacking fault energy (Bühler et al., 1963). The saturation stress as a function of temperature according to the algebraic form is plotted in Fig. 8b, and it is seen that the curves for different strain rates become more dispersed with increasing temperature, which is required to match the tensile test results. It should be added that an even higher temperature may result in a negative value of $\widehat{\tau}_{\mathrm{fs}}$ due to the choice of the algebraic form in Eq. (14), which is physically implausible. A method to deal with this issue can be found in Holmedal (2007). However, since the current work is conducted within the intermediate temperature range, the mathematically ill-posed but commonly applied algebraic form will not bring any numerical issues.

Secondly, even if the temperature effect is considered, the transition from negative to positive strain-rate dependence of the work hardening remains unsettled, and to accommodate this transition the solute effects must be included. It has been reported that the solute atoms affect the work hardening by suppressing the dynamic recovery processes, e.g. dislocation annihilation Deschamps et al., 1996; Kocks et al., 1985; Lloyd and Tangri, 1972). To account for this effect, the saturation mechanical threshold stress is taken to depend on the relative solute concentration c in the modified MTS model, cf. Eqns. (14) and ((15). Similar approaches can be found in several studies (Feng et al., 2017; Soare and Curtin, 2008). Another equivalent way of accounting for the solute and work hardening interaction can be found in the work of Ren et al. (2017), in which the solute's influence is directly integrated in the dynamic recovery term in Eq. (13). Fig. 9 shows the temperature dependence of the saturation stress for different strain rates as obtained with the power law form and algebraic form when DSA is accounted for. A transition from negatively to positively strain-rate dependant saturation stress is thus obtained, which agrees quite well with the experimental findings.

The predicted flow stress vs strain rate curves for various levels of plastic strain at different temperatures are shown in Fig. 10. For a fixed temperature, e.g., 298 K, the "N-shaped" curve will shift upwards with increasing strain due to the work hardening, see Fig. 10a. Owing to dynamic recovery and saturation of the work hardening, the spacing between adjacent curves decreases with strain. The flow stress vs strain rate curves are relatively flat at low strains, while the rate dependence becomes stronger with increasing strain. At higher temperatures, e.g., 418 K, the stress level becomes lower and the range of nSRS shifts towards increasing strain rates in Fig. 10b.

Fig. 11 shows the predicted flow stress vs temperature curves for various strain levels at 10^{-3} s^{-1} and 10^{2} s^{-1}. A rather flat curve is seen at 3% strain, whereas the temperature dependency becomes more pronounced with increasing strain, see Fig. 11a. Three regions can be observed: a stress decrease with increasing temperature in the low temperature range, a plateau within the intermediate temperature range, and then again a stress decrease with further increase of the temperature. Similar temperature dependence of the flow stress can also be found in other metals experiencing DSA, e.g. for titanium (Nemat-Nasser et al., 1999) and steel (Abed et al., 2017). With increasing strain rates, the plateau shifts in the direction of higher temperature, becomes weaker and vanishes. At the high strain rate, the flow stress vs temperature curves are monotonically decreasing at all strain levels, and the PLC effect will not occur, see Fig. 11b.

5.2. *Model predictions of strain-rate jump tests*

In the previous section, the alloy's behaviour under so-called "steady-state" conditions (Soare and Curtin, 2008) was investigated. The SRS can be measured by an abrupt strain rate jump at a given strain, as $S = \Delta\sigma/\Delta\ln\dot{\varepsilon}$. The "jump" can be upward (rate-increase) or downward (rate-decrease). Generally, the jumps in the two directions, up or down, are qualitatively similar despite some quantitative differences or asymmetries may occur (Klepaczko, 1975; Meng et al., 2019). In a recent work, a thorough study of complex loading paths' influence on the PLC effect was carried out, in which the strain rate jump tests are illustrated in detail (Ren et al., 2019). Here,

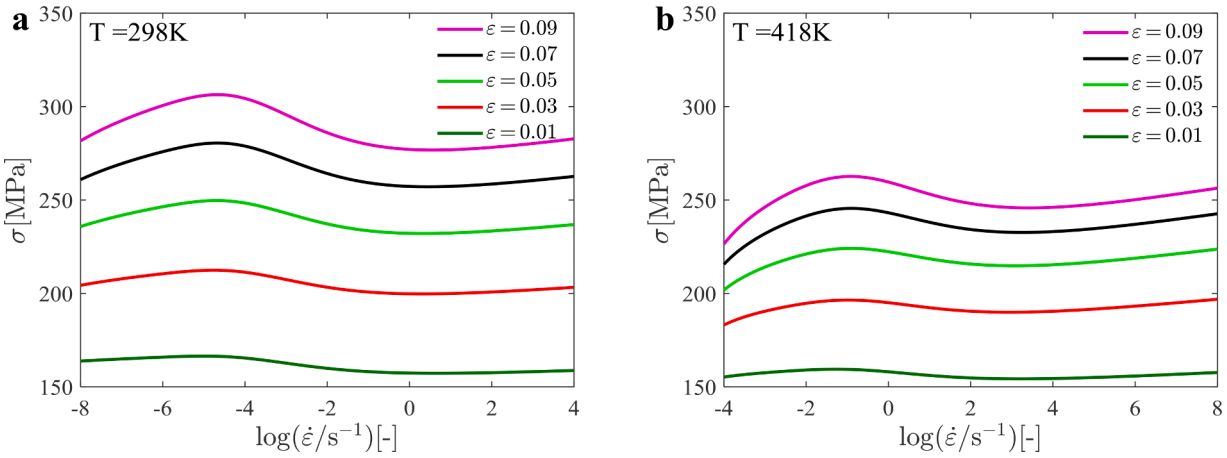

Fig. 10. Predicted flow stress vs strain rate curves for various levels of plastic strain at: (a) 298 K, (b) 418 K.

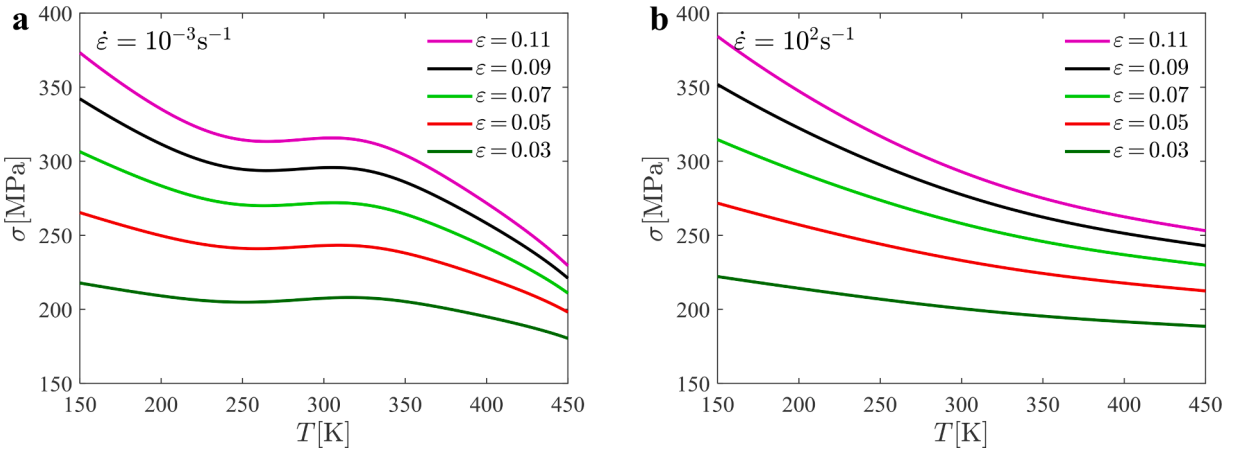

Fig. 11. Predicted flow stress vs temperature curves for various levels of plastic strain at: (a) 10^{-3} s^{-1}, (b) 10^{2} s^{-1}.

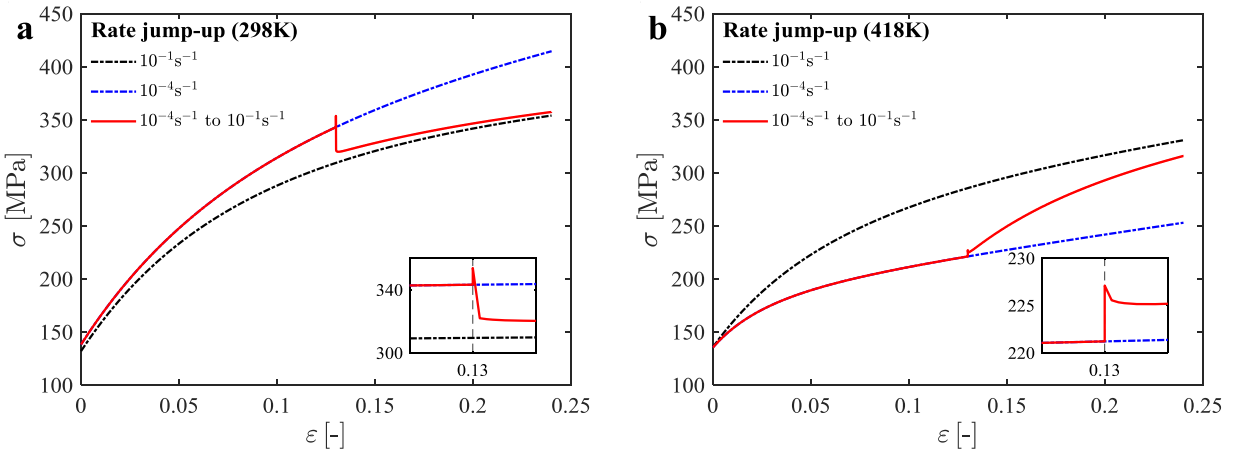

Fig. 12. Simulated stress responses in rate jump test with an abrupt strain rate change from 10^{-4} s^{-1} to 10^{-1} s^{-1} at 13% strain and temperature equal to (a) 298 K, (b) 418 K.

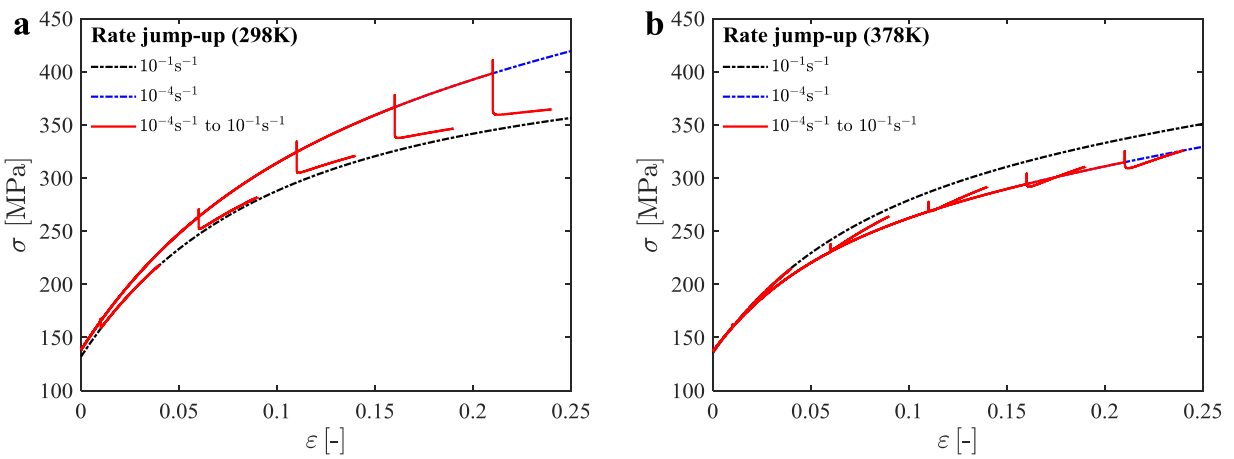

Fig. 13. Simulated stress responses during the rate jump tests with an abrupt strain rate change from 10^{-4} s^{-1} to 10^{-1} s^{-1} at 1%, 6%, 11%, 16%, and 21% strain and temperature equal to: (a) 298 K, (b) 378 K.

using the modified MTS model, a rate jump-up test is presented as an example, with an initial strain rate of $\dot{\varepsilon}_1 = 10^{-4}$ s^{-1}, followed by an abrupt strain rate increase to $\dot{\varepsilon}_2 = 10^{-1}$ s^{-1} at 13% strain. The model results of the jump-up tests at two selected temperatures are shown in Fig. 12, together with the curves for the two strain rates.

At 298 K, the alloy is inside the PLC domain, and a three-stage response is observed in Fig. 12a. An immediate stress increase ($\Delta\sigma_1 > 0$) implies a positive instantaneous SRS. This is in accordance with the thermal activation theory. Afterwards follows a short transient related to ageing, which obeys the ageing relaxation by Eq. (11), leading to a rapid stress decrease ($\Delta\sigma_2 < 0$). The sum of these two, i.e., $\Delta\sigma_1 + \Delta\sigma_2 < 0$, gives the alloy a negative steady-state SRS, as coined by McCormick (1988). This material response has been evidenced in the experimental study of Ren et al. (2019). Subsequently, a longer lasting work-hardening transient occurs, during which the stress approaches the new steady-state behaviour of the curve with the highest strain rate. Before the jump the dislocation densities are different. The evolution of the dislocation density towards the new steady-state level requires a considerable strain. More details concerning the material's response to a sudden strain rate change can be found in Xu et al., 2022a . At 418 K, the alloy's response to the rate jump is qualitatively similar as at 298 K, see in Fig. 12b. However, the material displays an instantaneous stress increase with a very small decrease afterwards, and the SRS is positive at this temperature, i.e., $\Delta\sigma_1 + \Delta\sigma_2 > 0$.

Fig. 13 shows predicted strain rate jump tests at different strains. At 298 K, an instantaneous positive stress increase followed by a subsequent stress decrease occurs for all strain levels, and the steady-state SRS remains negative at all calculated jump-strains in Fig. 13a. Note that magnitude of the instantaneous stress jump increases with increasing strain, which agrees with experimental findings for alloys exhibiting the PLC effect, such as AA6063 (Ling and McCormick, 1990) and AA5182-O (Picu et al., 2005). This phenomenon is widely observed in fcc metals, and is independent of the DSA, which requires a small strain contribution. An explanation was firstly proposed by Cottrell and Stokes (1955) and the phenomenon is captured by the MTS model. At 378 K, the SRS changes from slightly positive for the jumps at 1%, 6% and 11% strain, to slightly negative steady-state SRS for the jumps at 16% and 21% strain, see Fig. 13b. With further increase of the temperature, although not shown here, a positive steady-state SRS like in Fig. 12b prevails for the jump tests at all strains.

5.3. Strain rate sensitivity

Strain rate sensitivity is the key to the macroscopic behaviour associated with the PLC effect. As shown above, the SRS includes contributions from the instantaneous SRS, denoted S_i, and a transient SRS due to ageing, denoted S_a:

$$S = \frac{\partial\sigma}{\partial \ln\dot{\varepsilon}}\Big|_{\varepsilon} = S_i + S_a = \frac{\partial\sigma_f}{\partial \ln\dot{\varepsilon}}\Big|_{\varepsilon} + \frac{\partial\sigma_a}{\partial \ln\dot{\varepsilon}}\Big|_{\varepsilon} \tag{16}$$

The vanishing of the SRS, i.e., $S = 0$, is often used as the criterion for the occurrence of the PLC effect. Fig. 14 shows the predicted onset of instability. It is found that the zero SRS line does not agree quite well with the experimental observations. In contrast, the line with a lower SRS value of $S = -0.8$ MPa provides a better estimate of the critical strain. The result may stem from the fact that $S = 0$ is a necessary but not sufficient condition for the occurrence of the PLC effect. More refined criteria can be found in Mazière and Dierke (2012). Accurate predictions can be obtained by finite element simulations, which is beyond the scope of the current work. Besides, it has been shown that a very slight negative value of SRS is required for the instability to occur (Böhlke et al., 2009). Therefore, $S = 0$, will still be assumed as a rough estimate for occurrence of serrated flow and PLC bands in the following.

The strain rate sensitivity, S, is shown, for selected strains, as a function of strain rate for a given temperature in Fig. 15a and as a function of temperature for a given strain rate in Fig. 15b. In both plots, there exist regions of nSRS. In Fig. 15a, U-shaped S vs $\ln(\dot{\varepsilon})$ curves are found for all selected strains. Within the intermediate strain rate regime between 10^{-4}s^{-1} to 10 s^{-1}, the SRS is negative and decreasing with increasing strain. Similar curves have also been reported by Soare and Curtin (2008), but with two main differences compared to this work. Firstly, they predicted that the SRS decreases with strain for all strain rates, while here the SRS increases with

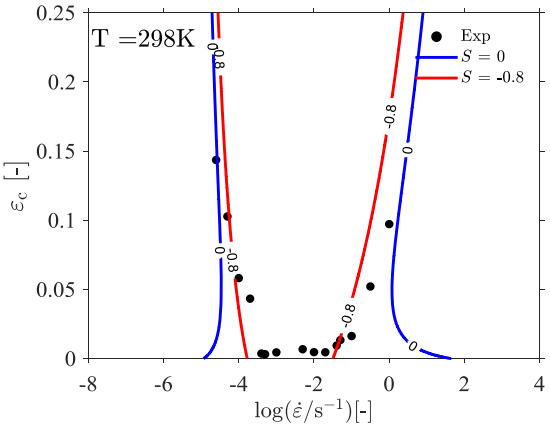

Fig. 14. Experimental (dots) and predicted (blue line with $S = 0$, red line with $S = -0.8$ MPa) critical strains at 298 K.

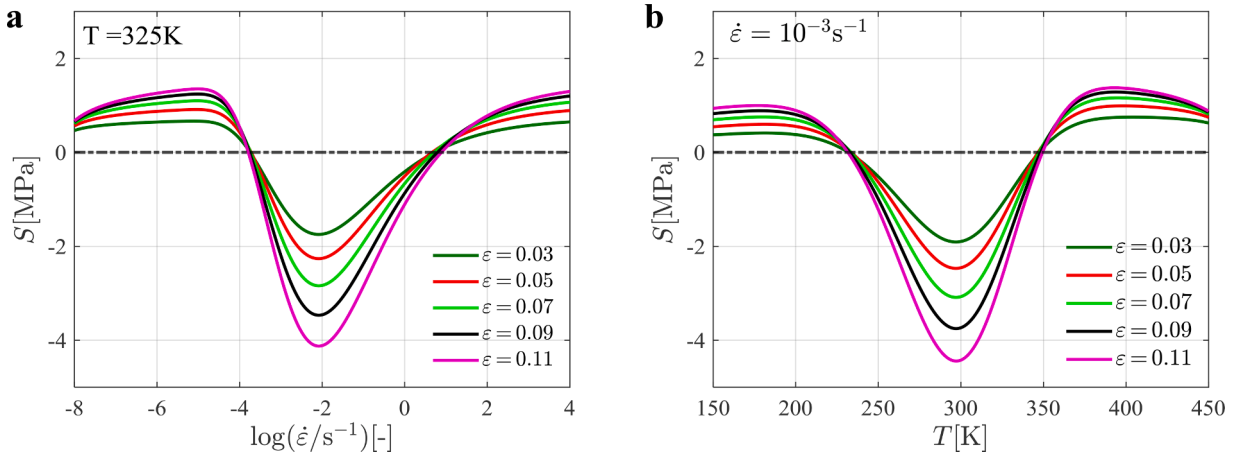

Fig. 15. Simulated strain rate sensitivity S as function of (a) strain rate and (b) temperature.

strain in the high and low strain rate ranges, as shown in Fig. 15a. This is reasonable because the strain ageing phenomenon is no longer "dynamic" at such high or low strain rates. In both cases the increased positive SRS origins from the MTS model and its description of the behaviour of alloys not exhibiting DSA. Many experimental observations support this behaviour (Bloom et al., 1985; Kocks et al., 1985; Mulford and Kocks, 1979). Secondly, it was shown by Soare and Curtin (2008) that by their model, the SRS equals zero in the low strain rate region but is positive non-zero at high strain rates. In contrast, the modified MTS model gives similar SRS at high and low strain rates, i.e., outside the DSA domain. The authors are not aware of experimental evidence for the vanishing SRS at low strain rates proposed by Soare and Curtin (2008).

As shown above, the SRS depends differently on strain inside and outside the PLC domain. To better investigate this, the contributions from the instantaneous SRS, S_i, and the transient ageing SRS, S_a, are compared in Fig. 16 as function of strain and strain rate. Here, the results at 325 K will be shown as an example. The increasing magnitude of the stress jumps with strain in the jump tests in Fig. 13 is due to that S_i increases with strain for all strain rates. The origin of this behaviour is the increase of $\widehat{\tau}_f$ with strain, magnifying the strain rate contribution through s, since $\tau_f = s(\dot{\gamma}, T)\widehat{\tau}_f$. In Fig. 16b, it is shown that for a given strain rate, S_a decreases with strain due to the strain dependant saturation ageing stress τ_{a0} defined by Eq. (9). Besides, the contour plot implies that DSA plays a more important role inside the PLC domain (intermediate strain rates) than outside the PLC domain (low and high strain rates). The superposition of contributions from S_i and S_a leads to the variation of S with strain and strain rate, inside and outside of the PLC domain, as shown in Fig. 17.

5.4. Jerky flow scenarios

Predicting the critical strain for onset of jerky flow is the most intriguing and challenging problem for alloys exhibiting DSA. As mentioned already, the normal and inverse behaviour of the critical strain can coexist in an alloy. In some cases, the serrations will even disappear at a certain level of strain, which is difficult to understand because it is commonly accepted that the influence of DSA

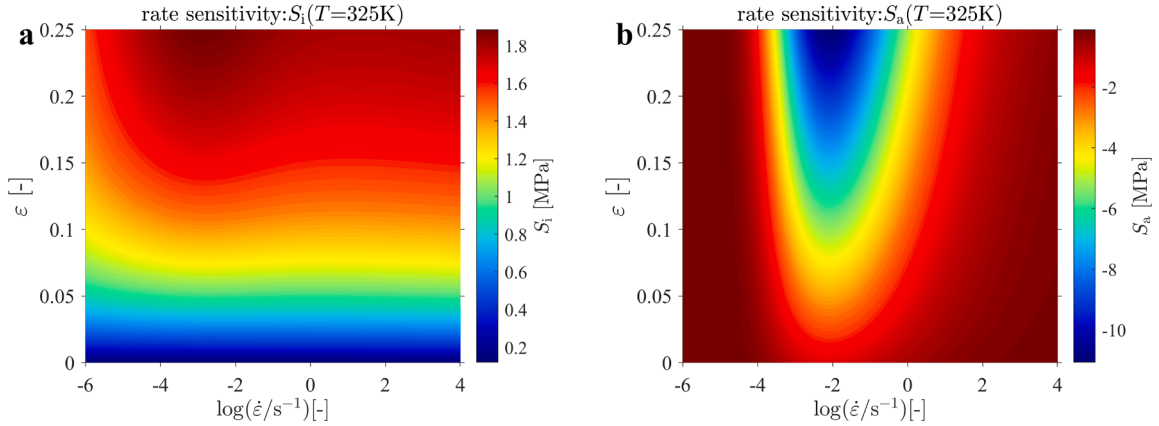

Fig. 16. (a) Instantaneous SRS, S_i, and (b) transient ageing SRS, S_a, at 325 K as a function of strain and strain rate. S_i increases with strain, while S_a decreases with strain.

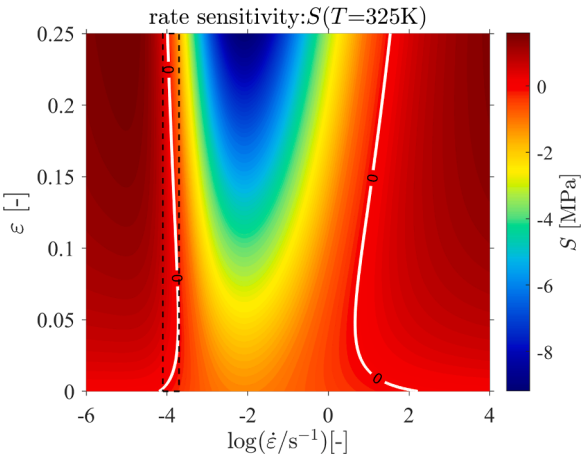

Fig. 17. Strain rate sensitivity S at 325 K as a function of strain and strain rate. The contour lines $S = 0$ are denoted by the white lines. S decreases with strain inside the PLC domain (intermediate strain rates), while it increases with strain outside the PLC domain (low and high strain rates).

increases with strain (Van den Beukel and Kocks, 1982). As far as we know, the only model that provides a consistent explanation of the complex behaviour of the critical strain is from Kubin and Estrin (1990), where the elementary strain Ω is assumed to be non-monotonically strain dependant due to the evolution of both mobile and forest dislocations. This key quantity gives the possibility to explain the different behaviours of the critical strain. However, available experimental data from Springer and Schwink (1995) suggests that the value of the elementary strain Ω increases monotonically at least for small strains, and an alternative explanation for the behaviour of the critical strain is given in the following.

As shown in Fig. 17, if the strain rate is either clearly inside or clearly outside the PLC domain, the behaviour of the material is well defined. However, if the strain rate is on the border of the PLC domain, even subtle changes in external conditions can make the jerky flow appear or disappear. Fig. 18 shows a zoom of the SRS map from Fig. 17 in the strain rate range between $10^{-4.1}$ s^{-1} and $10^{-3.7}$ s^{-1}, where three chosen strain rates are marked with vertical lines. The intersections between these lines and the contour line $S = 0$ are considered as the critical point for jerky flow. There are two distinct domains with negative steady-state SRS, which are merging into a single domain as the strain rate is increased. This type of behaviour has been observed for stress-strain curves at low strain rates from tests on a Cu-3.3 at.% Sn at 255°C (Kubin and Estrin, 1990; Räuchle et al., 1973). Such experimental data is scarce, because the strain rate (or temperature) window for this peculiar behaviour is narrow. Disappearance and reappearance of jerky flow was also observed in a Hastelloy X at 923 K (Sakthivel et al., 2012), where the tests were performed close to the upper temperature boundary for type C serrations to be observed. Similar phenomena may also occur around the upper strain rate (or lower temperature) boundary for the PLC effect but will be very difficult to observe without DIC measurements due to the light serrations at such high strain rates (or low temperatures).

Fig. 19 shows the evolution of the SRS in a simulated test with strain rate of 1.41×10^{-4} s^{-1}. It is seen that the sign of S changes twice during the test. The alloy is inside the PLC domain from the start, then moves outside for a while before it moves back in again. These results demonstrate that the competition between S_i and S_a can lead to this complex behaviour of the critical strain. The external testing conditions, i.e., strain rate and temperature, will decide the evolutions of both S_i and S_a with strain. Moreover, the initial microstructure of the alloy will also influence the S_i value and therefore play an important role on the behaviour of the critical strain. In the following analysis, the effect of the initial dislocation density will be investigated numerically.

The SRS maps for low and high values of the initial dislocation density are shown in Fig. 20. As illustrated in Fig. 20a, the line corresponding to a strain rate of 10^2 s^{-1} has only one intersection with the contour line $S = 0$, and it is seen that S is negative at low strains but turns positive at a strain of about 2%. This implies that the serrations will permanently disappear after a certain level of strain. There are many experimental observations of this behaviour of the critical strain (Guillot and Grilhe, 1972; Hayes, 1983; Hayes and Hayes, 1984; Max et al., 2014). The SRS map for a high initial dislocation density is shown in Fig. 20b. The initial value of S_i increases due to this change, which results in a higher initial value of S. In the low strain rate regime, the critical strain is seen to decrease with increasing strain rate, i.e., the "inverse" behaviour of the critical strain, whereas in the high strain rate range, the critical strain increases with increasing strain rate, i.e., the "normal" behaviour of the critical strain. For a strain rate of 10 s^{-1}, the SRS is first positive and then becomes negative at about 12% strain, which is consistent with most experimental observations with respect to the behaviour of the critical strain.

In summary, both S_i and S_a evolve with strain in the modified MTS model, which is the main difference between this model and the model of Kubin and Estrin (1990), where S_i is constant. As suggested by Van den Beukel and Kocks (1982), the evolution of the instantaneous SRS due to the microstructure evolution should not be overlooked. Although the instantaneous viscous response to a strain rate change determined by S_i does not contribute to the ageing effects, it does contribute to the strain rate sensitivity. The contributions S_i and S_a to the SRS are closely related to work hardening (or dislocation density) and dynamic strain ageing, respectively. The relative importance of these two contributions changes with strain and in some cases leads to a change in the sign of the

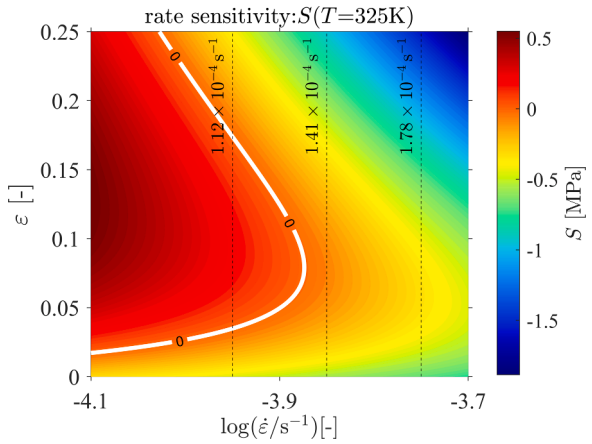

Fig. 18. Zoom of the SRS map within the region denoted by the dashed box in Fig. 17. At all three chosen strain rates, two distinct domains of nSRS are observed and the material exhibits a disappearance and reappearance scenario of jerky flow.

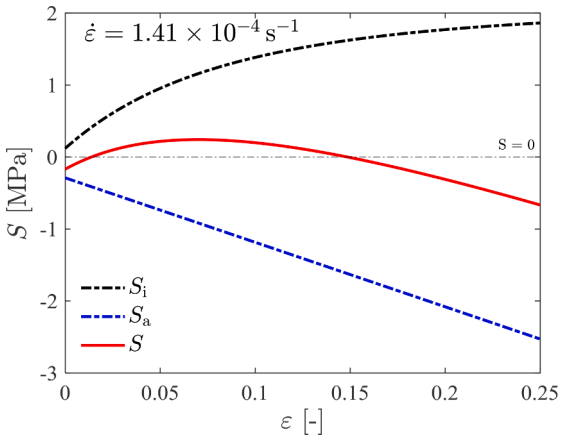

Fig. 19. Evolution of the SRS with strain for a prescribed strain rate of 1.41×10^{-4} s^{-1}, as shown in Fig. 18.

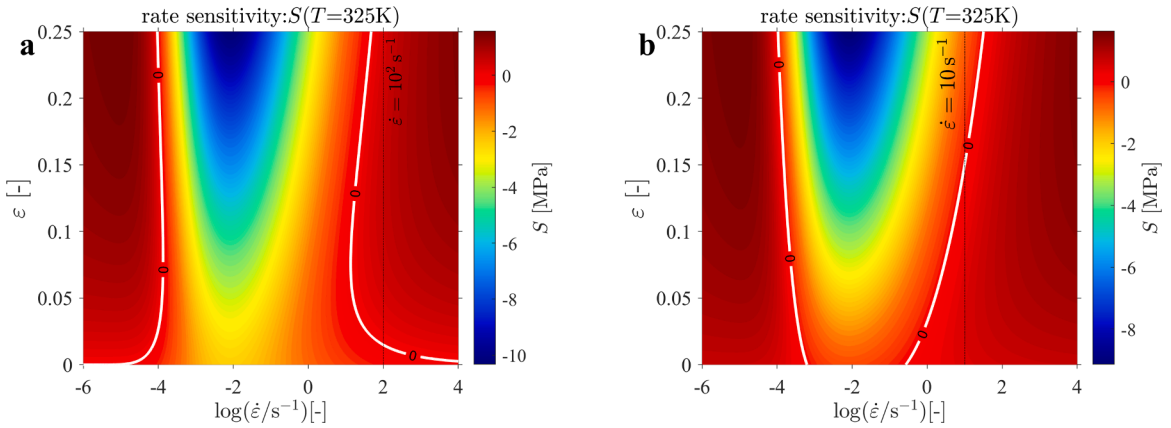

Fig. 20. Strain rate sensitivity S as a function of strain and strain rate at (a) a lower ($\hat{\tau}_{\mathrm{f\_ini}} = 0$ MPa) and (b) a higher ($\hat{\tau}_{\mathrm{f\_ini}} = 36$ MPa) initial dislocation density than in Fig. 17. In (a), the material shows the disappearance scenario of jerky flow at strain rate 10^2 s^{-1}. In (b), a well-defined critical strain is seen at strain rate 10 s^{-1}. Besides, both the normal and inverse critical strain behaviours are shown.

SRS. This competition between work hardening and dynamic strain ageing, which is influenced by testing conditions and initial microstructure, is the most fundamental reason for the complex behaviour of the critical strain.

5.5. PLC domain

Fig. 21 shows the predicted steady-state flow stress as function of the strain rate and temperature at a plastic strain of 10%, where the SRS is shown as a superimposed contour plot. It should be noted that the SRS is computed from Eq. (16), hence its value is not directly defined by the slope of the flow stress surface.

In Fig. 22, the domain in Fig. 21, where the steady-state SRS is negative, is projected onto the T^{-1} - $\dot{\varepsilon}$ plane. Similar plots can be found in Mesarovic (1995) and Soare and Curtin (2008). The contour lines $S = 0$ are highlighted to show the boundaries of the PLC domain. Along with the predictions obtained with the modified MTS model, the experimentally determined boundaries of the PLC domain for alloy AA5182-O from the current work and other studies (Abbadi et al., 2002; Picu et al., 2005) are also shown in the figure.

The predicted lateral boundaries of the nSRS domain are in excellent agreement with the experimental data. The two contour lines $S = 0$ at high and low temperature are nearly straight and essentially parallel with each other for the investigated range of inverse temperature and strain rate. For the lower boundary of the PLC domain, there is no experimental evidence due to the limit of the machine speed. As to the upper boundary, both experimental data from Abbadi et al. (2002) and Picu et al. (2005) are bounded with an almost horizontal line at $\dot{\varepsilon} = 10^{-1}\mathrm{s}^{-1}$. In contrast, the modified MTS model predicts no boundary at this strain rate. Additional tensile tests with strain rates of 0.5 s^{-1} and 1 s^{-1} were conducted at 298 K, and the results from these tests are depicted as the two open datapoints in Fig. 22. The material exhibited the PLC effect at both these strain rates.

Fig. 23 shows a comparison between the experimental stress-strain response at strain rates 10^{-4} s^{-1} and 1 s^{-1}. At the low strain rate, the onset of jerky flow is recognized both in the stress-strain curve and in the full-field DIC strain rate maps. However, at the high strain rate, the stress-strain curve is rather smooth, and an extremely high camera frame rate, up to 1000 Hz, was applied to capture the occurrence of the localization into a PLC band. Only a narrow strip of the specimen is covered by the camera to lower the storage size of the image and thus to improve the data collection rate. The data is saved in the computer memory rather than directly in the hard disk. This ensures the full capacity of the DIC system to capture the PLC band at such a high strain rate. As shown in Fig. 23, a PLC band clearly travels across the test specimen, which indicates that the PLC domain extends beyond a strain rate of 10^{-1} s^{-1} at room temperature.

5.6. Extension to Ni-based superalloys

Although the current work addresses the behaviour of an aluminium alloy, the main objective is to provide a general understanding of how to properly capture the PLC effect in the modelling. It would be highly interesting to test whether the current model is applicable to other materials. In this section, we will examine some major PLC characteristics of Ni-based superalloys as an example, whose microstructures and DSA regimes are completely different from aluminium alloys. A rough strain rate and temperature-dependant parameter calibration for the current model is firstly conducted and the prediction strengths of the model are shown afterwards. The reference data is mainly obtained for an X-750 Ni-based superalloy (Marsh and Kaoumi, 2017), but it also included some measured results from other similar superalloys. Fig. 24a shows both the experimental and fitted stress-strain curves for the heat-treated samples with stable microstructures comprised of γ' precipitation. In Fig. 24b, it is seen that the experimentally observed temperature-dependant yield stress can be well reproduced from 23 °C to 600 °C. Above 650 °C, an overestimation of the yield stress is observed, which is due to the emergence of other softening mechanisms (Marsh and Kaoumi, 2017). As illustrated by the model, this yield stress plateau within the intermediate temperature range stems from the "cancelling" temperature-dependant effects between decreasing ageing stress σ_a and increasing work hardening stress σ_f.

Fig. 25 shows the predicted and experimental scaling strain rate sensitivity parameter, $m = \partial \ln\sigma / \partial \ln\dot{\varepsilon}|_{\varepsilon,\ T}$, versus temperature at a

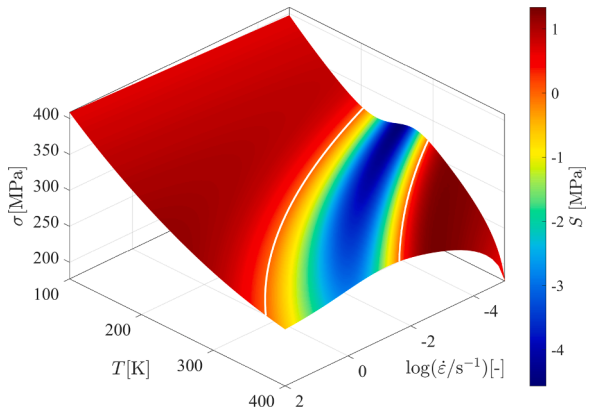

Fig. 21. Flow stress as function of strain rate and temperature at a strain of 10% with the SRS plotted as a superimposed contour map.

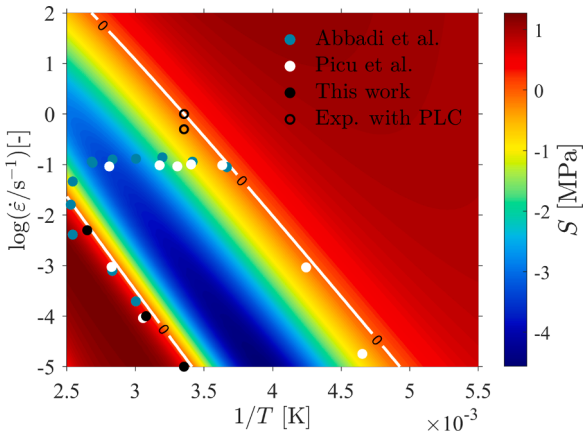

Fig. 22. Predicted steady-state SRS map on the inverse temperature and strain rate plane for a strain of 10% together with experimental data for the PLC domain from the current and other studies (Abbadi et al., 2002; Picu et al., 2005).

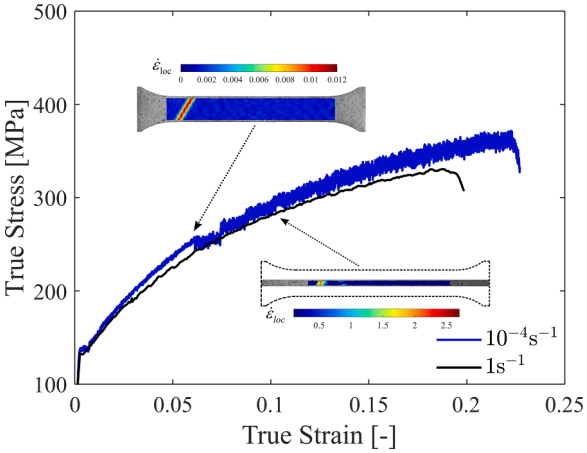

Fig. 23. True stress-strain curves at strain rate 10^{-4} s^{-1} and 1 s^{-1} along with strain rate maps from the DIC analysis.

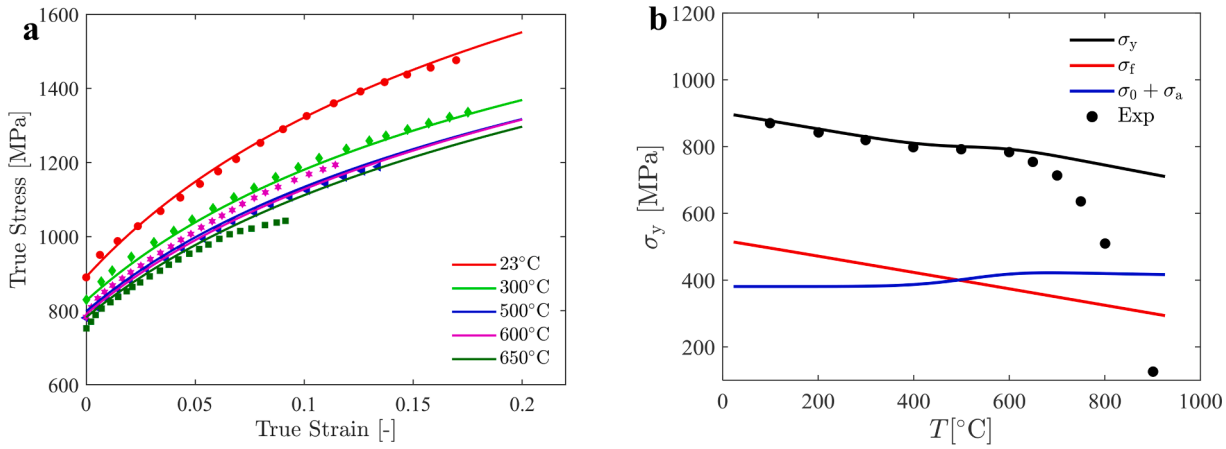

Fig. 24. (a) Stress-strain curves for various temperatures (b) yield stress versus temperature at 10^{-3} s^{-1}. Dots represent experimental datapoints of a X-750 Ni-based superalloy from Marsh and Kaoumi (2017) and solid lines represent calculations.

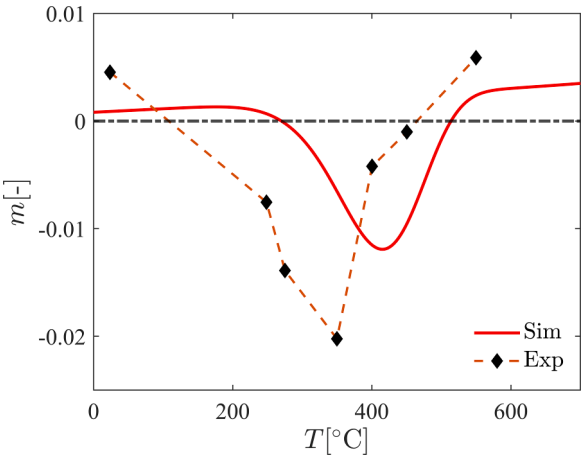

Fig. 25. Predicted strain rate sensitivity parameter m versus temperature at 10^{-5} s^{-1} for a strain of 5%. Discrete experimental datapoints are from a Ni-based 720Li superalloy (Gopinath et al., 2009), while the solid line represents the simulated behaviour.

strain rate of 10^{-5} s^{-1}. Based on the strain-rate jump test in a similar nickel-based 720Li superalloy (Gopinath et al., 2009), it is observed that the SRS is negative inside the PLC domain, while a positive SRS is seen outside the PLC domain. Similar results can also be found for Inconel 617 (Rao et al., 2019) and alloy 625 (Chatterjee et al., 2015) superalloys. A good qualitative agreement between simulation and experiment is reached, in which the SRSs inside and outside the PLC domain are given simultaneously. It is worth noting that the valley of the predicted U-shaped curvecentred at a higher temperature than what was observed in the experiments. This can be explained by the fact that PLC regime is strongly dependant on the testing conditions and the initial material state as discussed above.

The calibrated model can also be used to predict the critical strain at which PLC commences, similar as shown in Fig. 14. Fig. 26a shows both the experimental and predicted onset of instability. It is found that a lower SRS value, e.g., $S = -4$ MPa, provides a better estimate of the critical strain than the simple criterion of zero SRS. Again, a good qualitative agreement with the experimental data is obtained. Note, however, that the experimental critical strains in Marsh and Kaoumi (2017) are measured by occurrence of serrations instead of localization band from DIC analysis, which could be inaccurate. Only three data points are obtained, and it is difficult to conclude whether they belong to the "inverse" or "normal" critical strain range. Hence, the current calibration for this X750 alloy is not fine-tuned, due to the lack of experimental data, especially for the strain rate related parameters. More tests should be done to characterize the PLC strain rate boundaries to facilitate the calibration.

Another interesting result that can be obtained from the model, is the variation of the critical strain with temperature for given strain rates, as shown in Fig. 26b. It is seen that the predicted critical strain curve shifts towards higher strain rates (red arrow) with increasing testing temperature. This phenomenon has also been reported previously from a systematic experimental study on alloy 718 (Max et al., 2014). However, the observed critical strain ranges are between 0.3% and 2%, which is significantly lower than in the prediction. In another work based on alloy 720Li (Gopinath et al., 2009), a similar shift but with relatively higher critical strain values

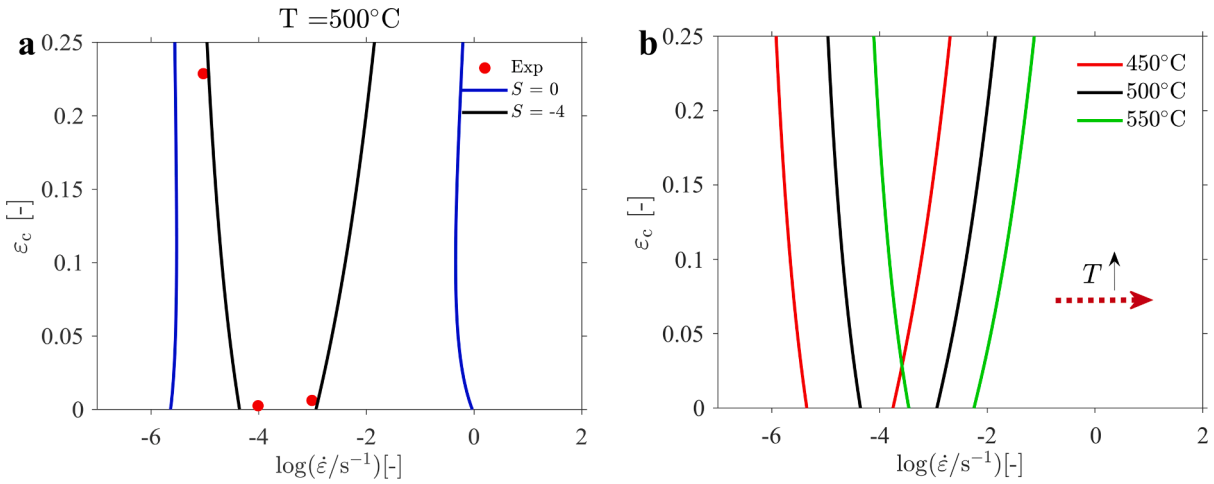

Fig. 26. (a) Experimental (dots) (Marsh and Kaoumi, 2017) and predicted (blue line with $S = 0$, black line with $S = -4$ MPa) critical strains at 500 °C, and (b) predicted variation of the critical strain with strain rate for given temperatures for an X-750 Ni-based superalloy.

(0.2% and 4%), was found for a low interstitial Ni-based superalloy. The existence of interstitial solutes (e.g., C, B) plays an important role on the dislocation pinning and may trigger an early onset of instabilities, while the current model is based on the "cross-core" diffusion mechanism for substitutionally strengthened alloys. The critical strain behaviour of materials that are strengthened by multiple elements in solid solution, either interstitials or substitutional, is yet not properly understood.

Fig. 27 shows the predicted PLC domain for the X-750 Ni-based superalloy (highlighted by white contour lines) plotted in the T^{-1}- $\dot{\varepsilon}$ plane, along with experimental results for a similar Ni-based 718 superalloy. Both the experiment and prediction give straight left boundaries at the high temperature range, however, the slopes of these lines are quite different. Choudhary (2014) showed that the solute content may affect the activation energy associated with serrated flow and therefore change the slope of the PLC boundary. Experimental measurements within the low temperature regime are still needed for a direct comparison with the constitutive model. There is no available experimental data for the upper boundary, due to the limitation of the traditional characterization method. However, it can be expected that the method proposed above may make it possible to detect the PLC effect in the high strain rate regime.

As for the Ni-based superalloy's behaviour under strain-rate jump tests, strain rate sensitivity evolutions or jerky flow scenarios, similar results are obtained, and the related discussions can be found in previous sections. Overall, the current model can provide a good qualitative description of the PLC effect for Ni-based superalloys, as compared to available experimental data, which substantiates the validity of the constitutive model proposed in this work. More experimental studies and further understanding of the deformation mechanisms are required for the utilization of the proposed constitutive model to other materials that are strengthened by both interstitial and substitutional solutes.

6. Conclusion

A systematic experimental and numerical study of the thermomechanical behaviour of the Al-Mg alloy, AA5182-O, has been conducted within the range of strain rates and temperatures where dynamic strain ageing is present. Experimental stress-strain curves and strain rate fields obtained by the DIC technique clearly reveal the influence of the temperature and strain rate on the serrated flow and the occurrence of PLC bands. A physically-based constitutive model, i.e., a modified version of the MTS model, is proposed and applied to accurately reproduce the alloy's thermomechanical behaviour. The main conclusions are summarized as follows:

- Dynamic strain ageing plays an important role on the work hardening behaviour of the alloy. The temperature and strain rate influence the effective solute concentration, which supresses dynamic recovery and leads to higher dislocation density at a given strain. Transitions from positive to negative and from negative to positive steady-state strain rate sensitivity are seen in the experiments and captured by the modified MTS model.
- The instantaneous and transient contributions to the steady-state strain rate sensitivity, the first caused by thermal activation and the latter by dynamic strain ageing, both evolve with strain. The sum of these two contributions results in a decreasing steady-state strain rate sensitivity with strain inside the PLC domain, while outside the PLC domain it increases with strain.
- A novel interpretation of the onset and termination of jerky flow is presented. The competition between work hardening and dynamic strain ageing is the most fundamental reason for the complex behaviour of the critical strain. The testing conditions (i.e., strain rate and temperature) and the initial microstructure (e.g., the dislocation density) greatly influence this competition and thus lead to different jerky flow scenarios.
- The proposed modified version of the MTS model provides maps of the steady-state strain rate sensitivity in terms of strain, strain rate and temperature. The domain of negative steady-state strain rate sensitivity or the PLC domain is accurately reproduced by this model. The results indicate that the PLC effect might prevail for higher strain rates than previously assumed in the literature.

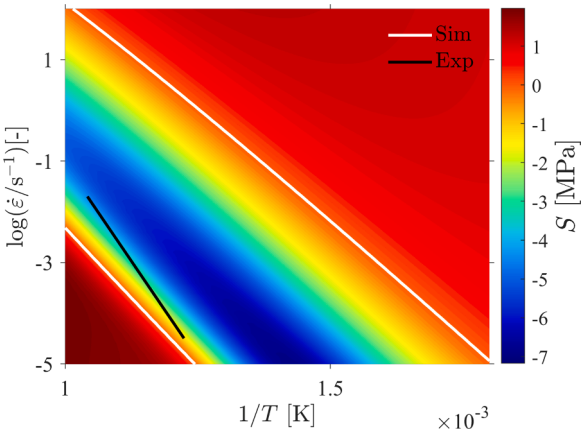

Fig. 27. (a) Simulated steady-state SRS map for a X-750 Ni-based superalloy on the inverse temperature and strain rate plane for a strain of 10%. (b) Experimental PLC domain for a Ni-based 718 superalloy (Max et al., 2014).

- The modified MTS model can be applied to other materials, e.g., Ni-based superalloys. A good qualitative agreement with experimental data from literature is reached. More accurate experimental studies and further theoretical understandings for the materials that contains both substitutional and interstitial solutes are suggested for the future work.

CRediT authorship contribution statement

Jianbin Xu: Investigation, Conceptualization, Methodology, Software, Formal analysis, Data curation, Writing – original draft, Writing – review & editing. **Bjørn Holmedal:** Conceptualization, Supervision, Writing – review & editing. **Odd Sture Hopperstad:** Conceptualization, Supervision, Funding acquisition, Writing – review & editing. **Tomáš Mánik:** Conceptualization, Supervision, Writing – review & editing. **Knut Marthinsen:** Conceptualization, Supervision, Funding acquisition, Project administration, Writing – review & editing.

Declaration of Competing Interest

The authors declare that they have no known competing financial interests or personal relationships that could have appeared to influence the work reported in this paper.

Acknowledgements

This research was conducted at the Centre for Advanced Structural Analysis (CASA), funded by the Research Council of Norway [grant number 237885] and several public and company partners.

Appendix: Material constants and parameters for the model

Symbol	Name	Unit	Value	Equation
Constants				
μ_0	shear modulus constant	MPa	29,573	(1)
D_0	empirical constant	–	0.112	(2)
T_0	empirical constant	K	215	(2)
b	Burgers vector	m	2.86×10^{-10}	(3)
α	interaction strength coefficient	–	0.34	(3)
k	Boltzmann constant	J/K	1.38×10^{-23}	(4)
Athermal stress parameter				
τ_0	athermal component	MPa	38.54	(1)
Work hardening parameters				
g_0	normalized structure evolution energy	–	1.34	(4)
p, q	thermal activation equation constant	–	2/3, 1	(4)
$\dot{\gamma}_0$	thermal activation equation constant	1/s	3×10^6	(4)
$\widehat{\tau}_{\mathrm{f\_ini}}$	initial value for structural evolution component	MPa	5.92	(13)
θ_0	initial hardening rate	MPa	415.42	(13)
κ	exponent constant for power law	–	1.29	(13)
$\widehat{\tau}_{\mathrm{fs0}}$	saturation structural evolution component	MPa	94.71	(14)
$g_{0\mathrm{s}}$	normalized saturate evolution energy	–	0.25	(14)
$\dot{\gamma}_{\mathrm{s0}}$	thermal activation equation constant	1/s	10^7	(14)
p_{s}, q_{s}	thermal activation equation constant	–	2, 1/4	(14)
$R^{'}$	Pre-factor in DSA	–	0.3	(15)
Dynamic strain ageing parameters				
$\widehat{\tau}_{\mathrm{a00}}$	initial saturation ageing stress	MPa	4.46	(9)
$\widehat{\tau}^{'}_{\mathrm{a00}}$	slope of reference saturation ageing stress evolution	MPa	46	(9)
$g_{0\mathrm{w}}$	normalized potential difference between dislocation interfaces	–	0.021	(9)
Ω	elementary strain increment	–	2.69×10^{-7}	(10)
ν_0	solute atom vibration frequency	1/s	3.8×10^{13}	(12)
$g_{0\mathrm{c}}$	normalized cross-core diffusion activation enthalpy	–	0.154	(12)
n	diffusion exponent	–	1/3	(5)

References

Abbadi, M., Hähner, P., Zeghloul, A., 2002. On the characteristics of Portevin–Le Chatelier bands in aluminum alloy 5182 under stress-controlled and strain-controlled tensile testing. Mater. Sci. Eng. A 337, 194–201.

Abed, F.H., Saffarini, M.H., Abdul-Latif, A., Voyiadjis, G.Z., 2017. Flow stress and damage behavior of C45 steel over a range of temperatures and loading rates. J. Eng. Mater. Technol. 139.

Belotteau, J., Berdin, C., Forest, S., Parrot, A., Prioul, C., 2009. Mechanical behavior and crack tip plasticity of a strain aging sensitive steel. Mater. Sci. Eng. A 526, 156–165.
Benallal, A., Berstad, T., Børvik, T., Hopperstad, O.S., Koutiri, I., de Codes, R.N., 2008. An experimental and numerical investigation of the behaviour of AA5083 aluminium alloy in presence of the Portevin–Le Chatelier effect. Int. J. Plast. 24, 1916–1945.
Bloom, T., Kocks, U., Nash, P., 1985. Deformation behavior of 4; Mo alloys. Acta Metall. 33, 265–272.
Böhlke, T., Bondár, G., Estrin, Y., Lebyodkin, M., 2009. Geometrically non-linear modeling of the Portevin–Le Chatelier effect. Comput. Mater. Sci. 44, 1076–1088.
Brechet, Y., Estrin, Y., 1995. On the influence of precipitation on the Portevin-Le Chatelier effect. Acta Metall. Mater. 43, 955–963.
Bühler, S., Lücke, K., Rosenbaum, F., 1963. Die durch Plastizitätsuntersuchungen bestimmte Stapelfehlerenergie von Silber im Temperaturbereich 172° K bis 873° K. Physica Status Solidi (B) 3, 886–900.
Chatterjee, A., Sharma, G., Tewari, R., Chakravartty, J., 2015. Investigation of the dynamic strain aging and mechanical properties in alloy-625 with different microstructures. Metall. Mater. Trans. A 46, 1097–1107.
Chen, S., Stout, M., Kocks, U., MacEwen, S., Beaudoin, A., 1998. Constitutive Modeling of a 5182 Aluminum As a Function of Strain Rate and Temperature. Los Alamos National Lab.. NM (United States).
Chen, S.R., Kocks, U., 1991. High-temperature Plasticity in Copper Polycrystals. Los Alamos National Lab. NM (United States).
Choudhary, B., 2014. Activation energy for serrated flow in type 316 L (N) austenitic stainless steel. Mater. Sci. Eng. A 603, 160–168.
Cottrell, A.H., Bilby, B., 1949. Dislocation theory of yielding and strain ageing of iron. Proc. Phys. Soc. London Sect. A 62, 49.
Cottrell, A.H., Stokes, R., 1955. Effects of temperature on the plastic properties of aluminium crystals. Proc. R. Soc. Lond. Series A Math. Phys. Sci. 233, 17–34.
Curtin, W.A., Olmsted, D.L., Hector, L.G., 2006. A predictive mechanism for dynamic strain ageing in aluminium–magnesium alloys. Nat. Mater. 5, 875–880.
Deschamps, A., Brechet, Y., Necker, C., Saimoto, S., Embury, J., 1996. Study of large strain deformation of dilute solid solutions of Al-Cu using channel-die compression. Mater. Sci. Eng. A 207, 143–152.
Fagerholt, E., 2012. Field measurements in mechanical testing using close-range photogrammetry and digital image analysis.
Feng, Y., Mandal, S., Gockel, B., Rollett, A.D., 2017. Extension of the Mechanical Threshold Stress Model to Static and Dynamic Strain Aging: Application to AA5754-O. Metall. Mater. Trans. A 48, 5591–5607.
Follansbee, P., Kocks, U., 1988. A constitutive description of the deformation of copper based on the use of the mechanical threshold stress as an internal state variable. Acta Metall. 36, 81–93.
Follansbee, P.S., 2014. Fundamentals of strength: principles, experiment, and Applications of an Internal State Variable Constitutive Formulation. John Wiley & Sons.
Fu, S., Cheng, T., Zhang, Q., Hu, Q., Cao, P., 2012. Two mechanisms for the normal and inverse behaviors of the critical strain for the Portevin–Le Chatelier effect. Acta Mater. 60, 6650–6656.
Gopinath, K., Gogia, A., Kamat, S., Ramamurty, U., 2009. Dynamic strain ageing in Ni-base superalloy 720Li. Acta Mater. 57, 1243–1253.
Guillot, J., Grilhe, J., 1972. Phenomene portevin-le chatelier dans les alliages al-mg a hautes temperatures, en fonction de la concentration. Acta Metall. 20, 291–295.
Hähner, P., 1997. On the critical conditions of the Portevin-Le Chatelier effect. Acta Mater. 45, 3695–3707.
Hayes, R., 1983. On a proposed theory for the disappearance of serrated flow in fcc Ni alloys. Acta Metall. 31, 365–371.
Hayes, R., Hayes, W., 1984. A proposed model for the disappearance of serrated flow in two Fe alloys. Acta Metall. 32, 259–267.
Holmedal, B., 2007. On the formulation of the mechanical threshold stress model. Acta Mater. 55, 2739–2746.
Jacobs, T.R., Matlock, D.K., Findley, K.O., 2019. Characterization of localized plastic deformation behaviors associated with dynamic strain aging in pipeline steels using digital image correlation. Int. J. Plast. 123, 70–85.
Kabirian, F., Khan, A.S., Pandey, A., 2014. Negative to positive strain rate sensitivity in 5xxx series aluminum alloys: Experiment and constitutive modeling. Int. J. Plast. 55, 232–246.
Keralavarma, S., Bower, A., Curtin, W., 2014. Quantum-to-continuum prediction of ductility loss in aluminium–magnesium alloys due to dynamic strain aging. Nat. Commun. 5, 1–8.
Klepaczko, J., 1975. Thermally activated flow and strain rate history effects for some polycrystalline FCC metals. Mater. Sci. Eng. 18, 121–135.
Klusemann, B., Fischer, G., Böhlke, T., Svendsen, B., 2015. Thermomechanical characterization of Portevin–Le Châtelier bands in AlMg3 (AA5754) and modeling based on a modified Estrin–McCormick approach. Int. J. Plast. 67, 192–216.
Kocks, U., Cook, R., Mulford, R., 1985. Strain aging and strain hardening in Ni-C alloys. Acta Metall. 33, 623–638.
Kocks, U., Mecking, H., 2003. Physics and phenomenology of strain hardening: the FCC case. Prog. Mater Sci. 48, 171–273.
Kreyca, J., Kozeschnik, E., 2018. State parameter-based constitutive modelling of stress strain curves in Al-Mg solid solutions. Int. J. Plast. 103, 67–80.
Kubin, L., Estrin, Y., 1990. Evolution of dislocation densities and the critical conditions for the Portevin-Le Chatelier effect. Acta Metall. Mater. 38, 697–708.
Lee, S.-Y., Takushima, C., Hamada, J.-i., Nakada, N., 2021. Macroscopic and microscopic characterizations of Portevin-LeChatelier effect in austenitic stainless steel using high-temperature digital image correlation analysis. Acta Mater. 205, 116560.
Ling, C., McCormick, P., 1990. Strain rate sensitivity and transient behaviour in an Al-Mg-Si alloy. Acta Metall. Mater. 38, 2631–2635.
Lloyd, D., Tangri, K., 1972. Dynamic strain ageing as a strengthening mechanism. Mater. Sci. Eng. 10, 75–80.
Louat, N., 1981. On the theory of the Portevin-Le Chatelier effect. Scr. Metall. 15, 1167–1170.
Mansouri, L., Thuillier, S., Manach, P., 2016. Thermo-mechanical modeling of Portevin–Le Châtelier instabilities under various loading paths. Int. J. Mech. Sci. 115, 676–688.
Marsh, C., Kaoumi, D., 2017. Serrated tensile flow in inconel X750 sheets: Effect of heat treatment. Mater. Sci. Eng. A 707, 136–147.
Max, B., Viguier, B., Andrieu, E., Cloue, J.M., 2014. A re-examination of the Portevin-Le Chatelier effect in alloy 718 in connection with oxidation-assisted intergranular cracking. Metall. Mater. Trans. A 45, 5431–5441.
Mazière, M., Dierke, H., 2012. Investigations on the Portevin Le Chatelier critical strain in an aluminum alloy. Comput. Mater. Sci. 52, 68–72.
McCormick, P., 1972. A model for the Portevin-Le Chatelier effect in substitutional alloys. Acta Metall. 20, 351–354.
McCormick, P., 1988. Theory of flow localisation due to dynamic strain ageing. Acta Metall. 36, 3061–3067.
Meng, C., Hu, W., Sandlöbes, S., Korte-Kerzel, S., Gottstein, G., 2019. The effect of large plastic deformation on elevated temperature mechanical behavior of dynamic strain aging Al-Mg alloys. Acta Mater. 181, 67–77.
Mesarovic, S.D., 1995. Dynamic strain aging and plastic instabilities. J. Mech. Phys. Solids 43, 671–700.
Mulford, R., Kocks, U., 1979. New observations on the mechanisms of dynamic strain aging and of jerky flow. Acta Metall. 27, 1125–1134.
Nemat-Nasser, S., Guo, W., Cheng, J., 1999. Mechanical properties and deformation mechanisms of a commercially pure titanium. Acta Mater. 47, 3705–3720.
Nes, E., 1997. Modelling of work hardening and stress saturation in FCC metals. Prog. Mater Sci. 41, 129–193.
Penning, P., 1972. Mathematics of the portevin-le chatelier effect. Acta Metall. 20, 1169–1175.
Pham, M.-S., Iadicola, M., Creuziger, A., Hu, L., Rollett, A.D., 2015. Thermally-activated constitutive model including dislocation interactions, aging and recovery for strain path dependence of solid solution strengthened alloys: Application to AA5754-O. Int. J. Plast. 75, 226–243.
Picu, R., 2004. A mechanism for the negative strain-rate sensitivity of dilute solid solutions. Acta Mater. 52, 3447–3458.
Picu, R., Vincze, G., Ozturk, F., Gracio, J., Barlat, F., Maniatty, A., 2005. Strain rate sensitivity of the commercial aluminum alloy AA5182-O. Mater. Sci. Eng. A 390, 334–343.
Picu, R., Zhang, D., 2004. Atomistic study of pipe diffusion in Al–Mg alloys. Acta Mater. 52, 161–171.
Portevin, A., Le Chatelier, F., 1923. Sur un phénomène observé lors de l'essai de traction d'alliages en cours de transformation. Comp. Rend. Acad. Sci. Paris 176, 507–510.
Rao, C.V., Srinivas, N.S., Sastry, G., Singh, V., 2019. Dynamic strain aging, deformation and fracture behaviour of the nickel base superalloy Inconel 617. Mater. Sci. Eng. A 742, 44–60.
Räuchle, W., Vöhringer, O., Macherauch, E., 1973. Der Portevin-Le Chatelier-effekt bei α-kupfer-zinn-legierungen. Mater. Sci. Eng. 12, 147–161.

Ren, S., Mazière, M., Forest, S., Morgeneyer, T.F., Rousselier, G., 2017. A constitutive model accounting for strain ageing effects on work-hardening. Application to a C–Mn steel. Comptes Rendus Mécanique 345, 908–921.
Ren, S., Morgeneyer, T., Mazière, M., Forest, S., Rousselier, G., 2019. Portevin-Le Chatelier effect triggered by complex loading paths in an Al–Cu aluminium alloy. Philos. Mag. 99, 659–678.
Ren, S., Morgeneyer, T., Mazière, M., Forest, S., Rousselier, G., 2021. Effect of Lüders and Portevin–Le Chatelier localization bands on plasticity and fracture of notched steel specimens studied by DIC and FE simulations. Int. J. Plast. 136, 102880.
Rusinek, A., Rodríguez-Martínez, J., 2009. Thermo-viscoplastic constitutive relation for aluminium alloys, modeling of negative strain rate sensitivity and viscous drag effects. Materials & Design 30, 4377–4390.
Sakthivel, T., Laha, K., Nandagopal, M., Chandravathi, K., Parameswaran, P., Selvi, S.P., Mathew, M., Mannan, S.K., 2012. Effect of temperature and strain rate on serrated flow behaviour of Hastelloy X. Mater. Sci. Eng. A 534, 580–587.
Sleeswijk, A.W., 1957. On the ductility of iron at 4.2-degrees-K. Acta Metall. 5, 764–765.
Sleeswyk, A., 1958. Slow strain-hardening of ingot iron. Acta Metall. 6, 598–603.
Soare, M., Curtin, W., 2008. Solute strengthening of both mobile and forest dislocations: The origin of dynamic strain aging in fcc metals. Acta Mater. 56, 4046–4061.
Song, Y., Garcia-Gonzalez, D., Rusinek, A., 2020. Constitutive models for dynamic strain aging in metals: Strain rate and temperature dependences on the flow stress. Materials 13, 1794.
Springer, F., Schwink, C., 1995. On a method to determine directly the waiting time of arrested dislocations and the elementary strain in dynamic strain ageing. Scr. Metall. Mater. 32, 1771–1776.
Swaminathan, B., Abuzaid, W., Sehitoglu, H., Lambros, J., 2015. Investigation using digital image correlation of Portevin-Le Chatelier Effect in Hastelloy X under thermo-mechanical loading. Int. J. Plast. 64, 177–192.
Taylor, G.I., 1934. The mechanism of plastic deformation of crystals. Part I.—Theoretical. Proc. R. Soc. Lond. Series A Contain. Pap. Math. Phys. Charact. 145, 362–387.
Van den Beukel, A., 1975. Theory of the effect of dynamic strain aging on mechanical properties. Physica Status Solidi (A) 30, 197–206.
Van den Beukel, A., Kocks, U., 1982. The strain dependence of static and dynamic strain-aging. Acta Metall. 30, 1027–1034.
Voyiadjis, G.Z., Song, Y., 2020. A physically based constitutive model for dynamic strain aging in Inconel 718 alloy at a wide range of temperatures and strain rates. Acta Mech. 231, 19–34.
Voyiadjis, G.Z., Song, Y., Rusinek, A., 2019. Constitutive model for metals with dynamic strain aging. Mech. Mater. 129, 352–360.
Wang, H., Berdin, C., Mazière, M., Forest, S., Prioul, C., Parrot, A., Le-Delliou, P., 2012. Experimental and numerical study of dynamic strain ageing and its relation to ductile fracture of a C–Mn steel. Mater. Sci. Eng. A 547, 19–31.
Wang, J., Guo, W.-.G., Gao, X., Su, J., 2015. The third-type of strain aging and the constitutive modeling of a Q235B steel over a wide range of temperatures and strain rates. Int. J. Plast. 65, 85–107.
Yuzbekova, D., Mogucheva, A., Zhemchuzhnikova, D., Lebedkina, T., Lebyodkin, M., Kaibyshev, R., 2017. Effect of microstructure on continuous propagation of the Portevin–Le Chatelier deformation bands. Int. J. Plast. 96, 210–226.
Zavattieri, P., Savic, V., Hector, L., Fekete, J., Tong, W., Xuan, Y., 2009. Spatio-temporal characteristics of the Portevin–Le Châtelier effect in austenitic steel with twinning induced plasticity. Int. J. Plast. 25, 2298–2330.
Xu, J., Hopperstad, O.S., Holmedal, B., Maník, T., Marthinsen, K., 2022b. On the spatio-temporal characteristics of the Portevin-Le Chatelier effect in aluminium alloy AA5182: an experimental and numerical study. To be published.
Xu, J., Holmedal, B., Hopperstad, O.S., Maník, T., Marthinsen, K., 2022a. Constitutive models for the Portevin-Le Chatelier effect in an AA5182 alloy. To be published.